

The Role of Indonesian Throughflow in a Global Ocean GCM

ANTHONY C. HIRST

CSIRO Division of Atmospheric Research, Aspendale, Victoria, Australia

J. S. GODFREY

CSIRO Division of Oceanography, Hobart, Tasmania, Australia

(Manuscript received 8 November 1991, in final form 5 June 1992)

ABSTRACT

The effect of the Indonesian Throughflow on the World Ocean circulation is examined by a series of experiments with a global ocean GCM. The principal objective is to gain an understanding of how ocean flows respond to the throughflow, and how these changes result in changes in the pattern of surface heat flux and sea surface temperature. Four model runs are conducted. The first run features an open Indonesian passage through which a nonzero net throughflow is permitted. The second run features a complete blockage of the Indonesian passage. The third run is designed to isolate the effects of purely buoyancy-driven throughflow: the Indonesian passage is open but the net volume transport is required to be zero. The fourth run is designed to isolate the effects of nonzero net throughflow on the Indian Ocean, independent of interocean buoyancy differences: the Indonesian passage is open but the throughflow water is cooled and salted toward profiles characteristic of the east Indian Ocean in the absence of throughflow.

Comparison of the first and second runs shows that the throughflow generally warms the Indian Ocean and cools the Pacific. However, large changes in the surface temperature and heat flux are restricted to certain well-defined regions: the Agulhas Current/outflow, the Leeuwin Current region off western Australia, the Tasman Sea, the equatorial Pacific, and two bands in the midlatitude South Pacific. In contrast, large subsurface temperature changes are widespread across both oceans. Heat budget analysis indicates that the large surface responses are dependent on the subsurface temperature change being brought to the surface, either by strong wind-forced upwelling (as in the equatorial Pacific) or by vigorous mixing in convective mixed layers (as in the other regions). Over most of both oceans, such mechanisms are absent and surface heat-flux changes are small (a few $W m^{-2}$). There, subsurface temperature perturbations are largely insulated from the surface and may extend via direct advection or baroclinic wave propagation. The additional heat is released upon encounter with upwelling or a convective mixed layer, which may be far removed from the source of the perturbation. Atlantic and far Southern Ocean effects are mostly very small, possibly because of our use of restoring upper boundary conditions. The third and fourth runs break the throughflow into its baroclinic and barotropic components. The baroclinic (buoyancy-driven) component affects surface heat flux strongly in the Leeuwin Current region but relatively weakly in the Agulhas Current and Tasman Sea. The barotropic component has the converse effect. Interocean heat exchange is discussed; the full throughflow transports a net 0.63 petawatts out of the Pacific Ocean, which represents about one-third of the total heat input into the model's equatorial Pacific.

1. Introduction

It has been suspected for some years that the Indonesian passages between the Pacific and Indian oceans have an effect on the global ocean circulation that is disproportionate to their small size. For example, Gordon (1986) suggested that North Atlantic Deep Water upwells and warms more or less uniformly throughout the World Ocean and that the major route by which this upwelled water returns to the Atlantic from the Pacific is through the Indonesian passages. Further, many authors have suggested that the input

of heat into the tropical Indian Ocean by the throughflow may significantly affect the Indian Ocean circulation and, at least regionally, the sea surface temperature and surface heat flux field (e.g., Godfrey and Golding 1981; McCreary and Kundu 1986).

Estimates of the volume of Indonesian Throughflow vary. Godfrey (1989) developed a Sverdrup model with detached islands that emphasized the potential role of Pacific winds in forcing the throughflow. His calculation yields a net throughflow of 16 ± 4 Sv ($1 \text{ Sv} \equiv 10^6 \text{ m}^3 \text{ s}^{-1}$) using annual-mean wind stress. Several more sophisticated numerical models find similar net transport (e.g., Cox 1975; Han 1984; Semtner and Chervin 1988), though others yield smaller values (e.g., Kindle et al. 1989). However, in the limit where the channel is wide and deep the Sverdrup estimate should be a

Corresponding author address: Dr. Anthony C. Hirst, Division of Atmospheric Research, CSIRO, Private Bag No. 1, Aspendale, Victoria, Australia.

good approximation. Recent observational work (e.g., Fieux et al. 1992) suggests that the annual-mean net throughflow is in fact more than 10 Sv. Such a flow can only return to the Pacific Ocean to the south of Tasmania, where the mean temperature is probably more than 10°C lower. The consequent heat transport of order ($10\text{ Sv} \times 10^{\circ}\text{C} =$) 0.4 petawatts from the Pacific to the Indian Ocean would be a substantial fraction of the total heat absorbed by the tropical Pacific Ocean (Talley 1984; Hsuing 1985). Further, the model simulations of Kindle et al. (1989) suggest that the throughflow may have significant interannual variation ($\pm 60\%$ of mean).

Thus, in the context of both global climate dynamics and interannual climate variability, it is appropriate to examine the effect of the passages on the global ocean in some detail. As first steps in this direction, Godfrey and Weaver (1991) and Hughes et al. (1991, referred to as GW and HWG) performed experiments with models featuring idealized Indian Ocean basins, open only via an "Indonesian passage" to a nominal Pacific Ocean. The Pacific temperature profile was prescribed to be either warm or cold. They showed that the Pacific can have substantial thermal effects on the Indian Ocean by flows through the Indonesian passage, even when net throughflow is zero. Baroclinic coastal Kelvin and Rossby waves radiating from the west Pacific can transport heat (and salt) even though their vertically integrated volume transport is identically zero. When the west Pacific is very warm, these waves supply heat to the Indian Ocean that is lost to the atmosphere over a very broad region, but particularly near southwestern Australia. The cooling off southwestern Australia creates large meridional steric height gradients in the GW and HWG models, both near the coast and for some hundreds of kilometers offshore. Earlier authors (e.g., Thompson 1984; Godfrey and Ridgeway 1985) showed that such gradients cause onshore geostrophic flow, downwelling, and coastal currents that flow directly into the prevailing wind. These conditions are in fact observed off western Australia, in the Leeuwin Current (Cresswell and Golding 1980). Godfrey and Weaver concluded that the unusual character of the Leeuwin Current, compared to other eastern boundary currents, should be attributed to thermal circulations driven remotely by Pacific heating and winds.

Godfrey and Weaver and HWG have emphasized one important role of the Indonesian passages: to allow adjustment of the Indian Ocean density profile towards that of the western Pacific via a purely baroclinic response, with zero net-volume transport through the Indonesian passages. The other important role of the passages is to permit a nonzero net transport of water from the Pacific to the Indian Ocean driven by Pacific winds. According to Sverdrup theory, this transport should proceed westward across the Indian Ocean, southward down the African coast, and eventually back to the Pacific south of Tasmania. Such a flow would

provide a strong, forced transfer of heat from the Pacific to the Indian Ocean, as discussed previously.

In this paper, we use a global ocean model to examine both the gross effect of nonzero net throughflow and the effect of purely baroclinic exchange of the type studied by GW and HWG. To do this, four model runs are conducted. The first, referred to as "run 1" or the "full throughflow case," features an Indonesian passage through which nonzero net throughflow is permitted (a net throughflow of 17 Sv develops). The second, referred to as "run 2" or the "no throughflow case," features a complete blockage of the Indonesian passage. The third and fourth runs are aimed at separating the effects of the pure baroclinic component and the net transport component of the throughflow. In "run 3," or the "baroclinic throughflow case," purely baroclinic exchange is permitted through the passage, but the net volume transport is required to be zero. In "run 4," or the "cooled throughflow case," a nonzero net throughflow is permitted, but the temperature and salinity of the throughflow water are adjusted back towards profiles typical of the model Indian Ocean between northwestern Australia and Java in the *no throughflow case*.

The grid resolution is much coarser than that used by GW and HWG, so eddies cannot be resolved nor can a Leeuwin Current be obtained that is realistically narrow and fast. In particular, the lack of a shallow continental shelf off the west Australian coast precludes the development of a barotropic component to the Leeuwin Current (Weaver and Middleton 1989). Nevertheless, the global scale of the model allows us to test whether climatic effects of the Indonesian throughflow may be felt farther afield than the tropical and eastern Indian Ocean. In particular, Godfrey and Golding (1981) noted that the throughflow must reduce the strength of the East Australia Current (EAC) and increase the strength of the Agulhas Current. One can anticipate that these effects will change the pattern of heat loss near both these currents. To further clarify our objectives, we show in Fig. 1a the surface heat flux field at the end of run 2, and in Fig. 1b the difference in surface heat flux between runs 1 and 2. The main aim of this paper is to understand the role of the throughflow in the mean mass and heat balances of the Indian and Pacific oceans, in particular how changes associated with the throughflow give rise to the heat flux difference pattern of Fig. 1b. It should be noted at the outset that we use restoring (i.e., Haney-relaxation type) upper boundary conditions on both temperature and salinity; this allows for direct comparison with the results of GW and HWG but places the issue of remote control of deep-water formation (e.g., Gordon 1986) outside the scope of the study.

Details of the model and experimental procedure are given in sections 2 and 3. The solutions for the four model runs are compared in section 4. Section 5 gives discussion on interbasin heat exchange and implications of the throughflow for the (atmospheric) cli-

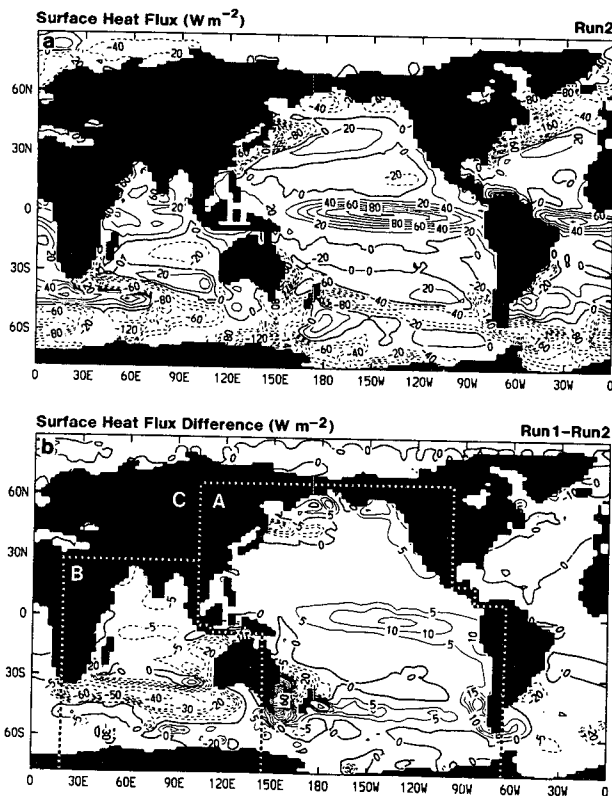


FIG. 1. Surface heat-flux fields for (a) run 2 and (b) difference between run 1 minus run 2. Units are $W m^{-2}$. Positive value indicates downward heat flux, that is, surface heat gain. (See Figs. 9c and 14c for blow-up of Indian/southwest Pacific sector.) Also shown in (b) are the ocean regions referred to in section 5a.

mate. Section 6 gives a summary and concluding remarks. The present paper presents only equilibrium solutions. The transient effects of throughflow variability on the World Ocean, which may be more relevant to interannual variability such as ENSO, are examined in Hirst and Godfrey (1993).

2. The model

a. Description of model

This study employs the Cox (1984) version of the Bryan-Cox ocean general circulation model, which is based on the primitive equation model described by Bryan (1969) and Bryan and Lewis (1979). In this study, the model domain consists of the World Ocean. The horizontal grid spacing is 1.5928° latitude by 2.8125° longitude. Fourier filtering is used north of $76^\circ N$. The model has 12 levels, at depths listed in Table 1. The polynomial approximation to the equation of state (Bryan and Cox 1972) is used.

The model topography for run 1 is shown in Fig. 2. In this case the model has eight islands: Antarctica, Madagascar, Philippines, Sulawesi, New Guinea, Australia, New Zealand, and Iceland. Nonzero depth-integrated circulation is permitted around each island [though transport between Australia and New Guinea is a realistically negligible 0.1 Sv, because of the shallow (50 m) sill depth]. The bottom topography field is derived from the Scripps $1^\circ \times 1^\circ$ dataset (Gates and Nelson 1975). The topography data were, first, interpolated to the model grid, then lightly smoothed. Finally, alterations were made by hand to improve representation of major ridges and sills, as indicated by the National Center for Atmospheric Research $5' \times 5'$ global topography dataset.

In run 2, the tropical Pacific and Indian oceans are isolated by a land bridge, which extends from the model's "Java Peninsula" to Australia via New Guinea (e.g., Fig. 9). In runs 3 and 4, the topography is identical to that in run 1. However, in run 3, no net flow is permitted between Australia and New Guinea and between New Guinea and Asia. This condition is implemented simply by equating the barotropic streamfunction values along the Australian and New Guinea coasts to the value (zero) along the Asian coast (e.g., after Manabe and Stouffer 1988).

No-slip conditions are applied at the lateral bound-

TABLE 1. Vertical spacing used in the experiments (depths in meters); also global-mean potential temperatures and salinities for each level from the model (end of experiment 1) and from observations (Levitus 1982).

Model layer	Depth of		Δz	Model		Observed	
	Middle	Bottom		T ($^\circ C$)	S (psu)	T ($^\circ C$)	S (psu)
1	13	25	25	18.126	34.736	17.98	34.73
2	38	50	25	17.711	34.771	17.39	34.85
3	70	90	40	17.194	34.808	16.14	34.96
4	125	160	70	16.308	34.841	13.95	35.03
5	215	270	110	15.153	34.887	11.57	34.97
6	370	470	200	13.365	34.832	8.93	34.80
7	635	800	330	11.145	34.727	6.19	34.63
8	1025	1250	470	8.916	34.607	4.11	34.62
9	1575	1900	650	6.872	34.513	2.87	34.70
10	2350	2800	900	5.244	34.453	2.06	34.74
11	3250	3700	900	3.554	34.347	1.61	34.74
12	4150	4600	900	2.952	34.307	1.34	34.73

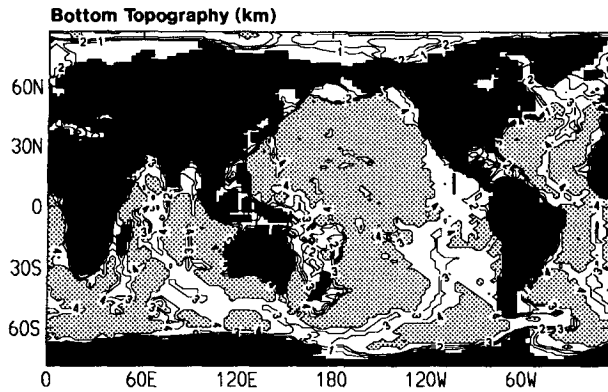


FIG. 2. Model bottom topography; contour interval 1000 m.

aries. Bottom stress (τ_b^x, τ_b^y) is added via a linear drag law after Toggweiler et al. (1989):

$$(\tau_b^x, \tau_b^y) = \rho_0 C_b (u_b, v_b), \quad (1)$$

where u_b and v_b are the eastward and northward bottom-level velocity components. The value of the bottom drag coefficient C_b (Table 1) is based on a linearization of the quadratic drag formula, assuming a quadratic drag coefficient of 2.5×10^{-3} (e.g., Hunter and Hearn 1988) and a typical bottom current speed of $2 \times 10^{-2} \text{ m s}^{-1}$.

Values assigned to the model parameters are listed in Table 2. The eddy diffusivities and viscosities are spatially constant. After some experimentation, we followed HWG in our choice of the rather large values for the vertical eddy viscosity (A_{MH}) and diffusivity (A_{TV}) and for the same numerical reasons. However, the large A_{TV} leads to excessively deep and diffuse pycnocline structure, which is reflected in the model's global-mean temperature profile for run 1 shown in Table 1. The resulting deep baroclinic zone leads to excessively deep current structure generally, and an Antarctic Circumpolar Current (ACC) that is too strong in total volume transport by about a factor of 2. The weak density structure also results in midlatitude convection penetrating to excessive depth. On the other hand, the large A_{TV} offsets the diminution of poleward heat transport associated with the required large horizontal eddy viscosity (Bryan 1987). The poleward heat transport in the present model is of realistic order [e.g., compare our Fig. 20 with Fig. 3 of Hsuing (1985)].

The model uses the Cox (1987) parameterization to compute vertical diffusion and convection implicitly, and the enhanced vertical diffusivity in regions of static instability is set at $10 \text{ m}^2 \text{ s}^{-1}$. No parameterization is included for deepening the surface mixed layer by wind-forced mixing. Convection resulting from static instability is, thus, the only mechanism for mixed-layer deepening.

b. Upper-boundary forcing

The ocean model is forced at its upper surface by annual-mean climatological wind stress and by heat flux and salinity variations as discussed below. The wind stress used is the Hellerman and Rosenstein (1983) climatology. The net surface heat flux (F_N) is calculated as a sum of the sensible (F_S), latent (F_L), and net radiative (F_R) heat fluxes; that is,

$$F_N = F_S + F_L + F_R, \quad (2)$$

where

$$F_S = \rho_a C_{pa} C_H V_a (T_a - T_1) \quad (3a)$$

$$F_L = \rho_a L C_E V_a (q_a - q_s(T_1)). \quad (3b)$$

Here, T_1 is the ocean temperature at the top model level (also referred to as the model SST). Other symbols have their usual meanings. The surface air temperature (T_a), specific humidity (q_a), wind speed (V_a), and net radiation (F_R) are all specified from the annual mean climatology of Esbensen and Kushnir (1981). Apart from the nonlinearity in $q_s(T_1)$, (2) and (3) are equivalent to a Haney relaxation towards a passive equilibrium temperature (T_e) (e.g., Han 1984). The value of T_e depends on the prescribed F_R , V_a , T_a , and q_a and is shown for the globe in Fig. 3a. Generally T_e lies within 3°C of the observed and modeled SSTs. The effective relaxation time constant for small perturbation (γ_H) depends primarily on V_a and $\partial q_s / \partial T$ and is shown for the globe in Fig. 3b. In ice-covered regions, the model top-level temperature is instead explicitly relaxed back towards the Levitus (1982) climatological values, with an e -folding time scale of 20 days.

Large systematic differences are found between the Esbensen-Kushnir SSTs and the SST climatologies of Levitus (1982) and Reynolds and Roberts (1987) in ice-free regions poleward of about 55°S and 65°N .

TABLE 2. Standard values of model coefficients.

Parameter	Symbol	Value
Horizontal diffusivity	A_{TH}	$1 \times 10^3 \text{ m}^2 \text{ s}^{-1}$
Horizontal viscosity	A_{MH}	$1 \times 10^5 \text{ m}^2 \text{ s}^{-1}$
Vertical diffusivity	A_{TV}	$1 \times 10^{-4} \text{ m}^2 \text{ s}^{-1}$
Vertical viscosity	A_{MV}	$20 \times 10^{-4} \text{ m}^2 \text{ s}^{-1}$
Density of air	ρ_a	1.22 kg m^{-3}
Density of ocean water	ρ_0	1025 kg m^{-3}
Heat capacity of air	C_{pa}	$1 \times 10^3 \text{ J kg}^{-1} \text{ K}^{-1}$
Heat capacity of water	C_w	$4 \times 10^3 \text{ J kg}^{-1} \text{ K}^{-1}$
Latent heat of vaporization	L	$2.46 \times 10^5 \text{ J kg}^{-1}$
Bottom drag coefficient	C_B	2.5×10^{-3}
Dalton number	C_H	1.0×10^{-3}
Stanton number	C_E	1.5×10^{-3}
Thermal relaxation coefficient ^a	γ_T	$5.79 \times 10^{-7} \text{ s}^{-1}$
Salinity relaxation coefficient ^b	γ_S	$2.89 \times 10^{-7} \text{ s}^{-1}$

^a For top level under ice; ^b For top level globally.

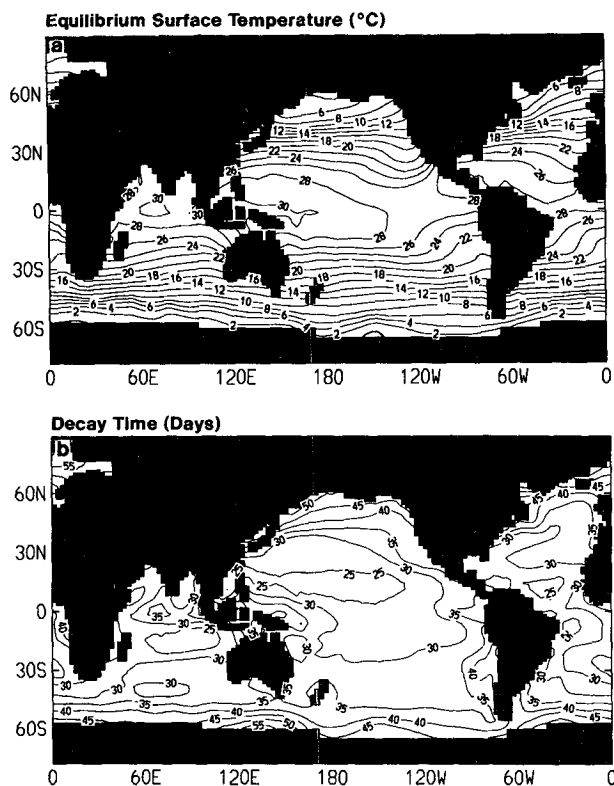


FIG. 3. Haney relaxation constants implied by thermal upper boundary condition: (a) passive equilibrium temperature ($^{\circ}\text{C}$) and (b) relaxation time constant (days).

These differences (which are up to 5°C) are reflected in the Esbensen–Kushnir T_a and q_a . The Esbensen–Kushnir values in these regions are thus suspect. In affected regions, we use a “corrected” T_a obtained by subtracting the difference between the Esbensen–Kushnir SST and Levitus SST from the Esbensen–Kushnir T_a and a “corrected” q_a obtained by maintaining the relative humidity implied by the Esbensen–Kushnir data.

The effective Haney relaxation time constant (Fig. 3b) lies mostly in the range 25–40 days; corresponding to a Haney flux coefficient in the range $46\text{--}28 \text{ W m}^{-2} \text{ }^{\circ}\text{C}^{-1}$. Our relaxation time scales are slightly larger than those implied by the analysis of Han (1984), possibly because of his inclusion of an idealized radiation response. However, both this study and that of Han (1984) assume constant T_a and q_a . We note that SST changes in the real ocean would be expected to produce changes in T_a and q_a in the same sense, so that restoring heat flux changes may be considerably reduced (e.g., Seager et al. 1988). Consequently, the most realistic Haney relaxation time scales may be even longer than those implied by the present scheme.

In the present study, we simply relax the model top-level salinity (S_1) back towards values (S_L) interpolated

from the Levitus (1982) annual-mean climatology. In effect, a salinity flux F_S of form is provided:

$$F_S = \rho_0 \Delta z_1 \gamma_S (S_L - S_1). \quad (4)$$

The relaxation time scale (γ_S) is set at $(40 \text{ days})^{-1}$. In reality, the freshwater flux from evaporation/precipitation is largely independent of the underlying salinity; thus, the upper boundary condition on salinity is more like fixed-flux than relaxation (Welander 1986; Maier-Reimer et al. 1990; Weaver and Sarachik 1991). A restoring boundary condition on salinity is used because we wished to limit the study primarily to the direct first-order effects of Indonesian throughflow on the heat and mass budgets of the Indian and Pacific oceans. Large remote changes in salinity might occur in GCMs forced with a fixed salinity flux, possibly having a major effect on thermohaline overturning. Such changes would likely be much diminished in GCMs forced with a restoring condition. However, GCMs forced with fixed salinity flux can display very idiosyncratic behavior (Bryan 1987; Weaver and Sarachik 1991; Marotzke 1991). For this and other reasons (section 5b), we expect long-range changes occurring under a fixed salinity-flux boundary condition to be very model dependent.

Our upper-boundary restoration imposes some imprint of the throughflow on the model surface fields even in the “no throughflow” case. For example, S_L features a salinity minimum stretching across the tropical south Indian Ocean (Fig. 22 of Levitus 1982). We tested the model sensitivity to this imprint by conducting a run identical to run 2 except that S_L was adjusted upward to 35.3 psu throughout the Indian Ocean between 5°S and 20°S . In addition, T_a and q_a were adjusted so that the effective T_e was reduced by 0.3°C in the west of this region ramping to a 1.0°C reduction in the east. The effect on surface heat flux and circulation was small; in particular, the Leeuwin Current features of run 2 were only slightly weakened.

No attempt has been made to correct the polar values of Levitus annual-mean salinity so as to reflect relatively high wintertime salinities (cf. England 1992). Consequently, the model’s polar waters are too fresh, and this contributes to the low values of globally averaged salinity for the deep levels (Table 1).

The differences between the model and observed (Levitus 1982) top-level temperature and salinity fields are shown in Figs. 4a and 4b, respectively. Model fields are for the case of Indonesian passage open. The model SST departs from observations generally by less than 2°C . The model surface salinity deviates from observations by generally less than 0.3 psu, except in some near-coastal regions.

c. Prescription of Indonesian topography

In a series of preliminary runs, that featured an Indonesian passage of a width of four velocity grid points,

the net throughflow was found to be strongly dependent on the prescribed depth of the Indonesian sill. Sill depths in the range 1250–2800 m yielded throughflows in the range 21–24 Sv. A greater sill depth (3700 m) yielded 16 Sv, similar to that expected from a Sverdrup model (Godfrey 1989). The enhancement of throughflow in those runs with shallower sills appears to result from a thermohaline effect: interocean density differences at depths below the sill (Table 3) may generate cross-sill pressure gradients that strengthen the throughflow. Throughflows in the range 21–24 Sv are considerably larger than recent annual-mean estimates of order 10–15 Sv based on observations (Godfrey 1989; Fieux et al. 1992). Further, the throughflow in the preliminary runs is southward at all available levels above 1800 m, which is much deeper than the 500 m or so inferred from observations (e.g., Wyrki 1962; Hamon 1965; Fieux et al. 1992). Our purpose is not to accurately model the throughflow per se but only to study its effect on the large-scale circulation. Therefore, we simply prescribe an Indonesian sill of 800-m depth, which yields a more realistic throughflow of 17.1 Sv. An explicit Sulawesi and an extended “Java Peninsula” is included. The channel to the west and south of Sulawesi is 800 m, that between Sulawesi and New Guinea

TABLE 3. Differences between quantities averaged over area *A* [west Pacific; see section 4a(4)] and area *B* (east Indian) at each model level, for the indicated runs. Here ΔT , ΔS , and $\Delta \rho$ denote differences (area *A* minus area *B*) for potential temperature, salinity, and density, respectively.

Level	Depth (m)	ΔT	ΔS	$\Delta \rho$ (kg m^{-3})		
		(Run 2) ($^{\circ}\text{C}$)	(Run 2) (psu)	(Run 2)	(Run 1)	(Run 3)
1	13	1.42	-0.12	-0.56	-0.34	-0.37
2	38	2.01	-0.22	-0.80	-0.36	-0.43
3	70	2.47	-0.28	-0.96	-0.37	-0.40
4	125	2.98	-0.30	-1.09	-0.34	-0.43
5	215	2.97	-0.36	-1.06	-0.21	-0.45
6	370	1.56	-0.49	-0.73	-0.02	-0.39
7	635	-0.22	-0.57	-0.39	-0.04	-0.23
8	1025	-0.61	-0.39	-0.19	-0.00	-0.27
9	1575	-0.65	-0.22	-0.05	-0.09	-0.06
10	2350	-0.35	-0.12	-0.03	-0.06	-0.08
11	3250	-0.51	-0.04	-0.13	-0.15	-0.11
12	4150	-0.61	-0.03	-0.15	-0.16	-0.13

is 270 m deep. The Timor Strait (between the Java Peninsula and Australia) is 1250 m deep.

3. Experimental procedure

Run 1 was initialized with uniform salinity (34.7 psu) and a temperature distribution based on the zonally averaged Levitus (1982) data, and at rest. Acceleration techniques of Bryan (1984) were used to speed convergence of the model solution. The barotropic streamfunction and baroclinic velocity equations were integrated with a time step of 20 min. The time step for the potential temperature (T)¹ and salinity (S) equations varied with depth, being set at 1.5 days for levels 1–7 and steadily increased at lower levels to 6 days at level 12. Experiments to determine the effect of acceleration techniques on the final solution are briefly discussed in the Appendix.

The integration for run 1 proceeded in two stages. In the first stage, the model was run for 440 000 time steps (i.e., about 1800/7200 yr for upper/lower T and S). During this stage, several minor adjustments were made to the model topography and parameters. In the second stage, the model was configured exactly as described in section 2, and run for a further 130 000 steps (530/2120 yr).

At the end of stage two, very small systematic adjustments are still occurring in the deep-ocean fields. Since it is impossible to integrate to a completely equilibrated solution in finite time, we define the following convergence criterion: the solution is considered converged if rates of change of the global-mean temperature and salinity at each level are less than $5 \times 10^{-3} \text{ }^{\circ}\text{C}$

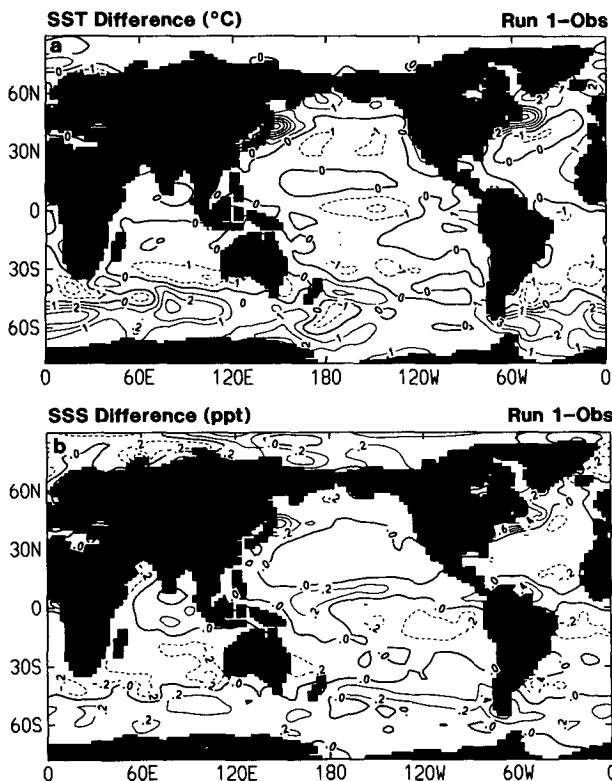


FIG. 4. Difference between modeled (run 1) and observed (Levitus 1982) fields at the top model level: (a) temperature ($^{\circ}\text{C}$) and (b) salinity (psu).

¹ Henceforth, potential temperature is simply referred to as “temperature.”

$(100 \text{ yr})^{-1}$ and $1 \times 10^{-3} \text{ psu } (100 \text{ yr})^{-1}$. Final rates of change for stage two satisfy this criterion. Apart from the small drift, the only time-dependent aspects of the solution at the end of stage two are (i) intermittent convection at some individual grid points and (ii) very weak oscillatory behavior evident in some regions (primarily the far north Pacific and Atlantic and the Southern Ocean). However, all fields shown here are for the final time step of each run; the effect of transients on model fields is found to be too small to warrant time averaging.

Runs 2–4 were initialized using the temperature and salinity fields from run 1 at step 70 000 of stage two. The T and S fields were held constant for the first 1600 time steps to allow velocity fields to spin up. The integrations then proceeded using the depth-dependent scalar time stepping for 80 000 steps (330/1320 yr). The final residual drifts for each of the four runs satisfy the convergence criterion given previously. Moreover, plots of departures from run-1 fields changed little after about 30 000 steps (125/500 yr). Several ancillary model runs have also been conducted and are detailed where referenced.

4. Results

a. Model climatology

1) GLOBAL

Before discussing the effect of opening or closing the Indonesian passage, it is appropriate to briefly review salient aspects of the ocean model's climatology that are common to both runs 1 and 2. Aspects of the global climatology are presented in this subsection. More detailed discussions for the Indian and South Pacific oceans are presented in the following subsections.

The streamfunction of depth-integrated flow is presented in Fig. 5 for (a) run 1 and (b) run 2. The strengths and locations of the gyres and equatorial currents are broadly consistent with Sverdrup dynamics (e.g., Godfrey 1989), with the major exception being the almost complete retroflexion of the Agulhas Current off southern Africa. The general pattern matches well that inferred by Godfrey (1989) from Levitus (1982) observations (with the exception of the excessive ACC transport). The course of the Antarctic Circumpolar Current (ACC) is strongly influenced by bottom topography, in particular, the Kerguelen Ridge (at about 70°E) and the New Zealand Plateau.

The surface pressure fields are shown in Fig. 6 for (a) run 1 and (b) run 2, while Fig. 6c shows the surface steric height of the World Ocean based on Levitus (1982) observations and an assumed 2000-m depth of no motion. The modeled and observed patterns agree quite well qualitatively, an exception being the poor simulation of the observed steric height minimum centered at about 8°N in the Pacific. The geostrophic

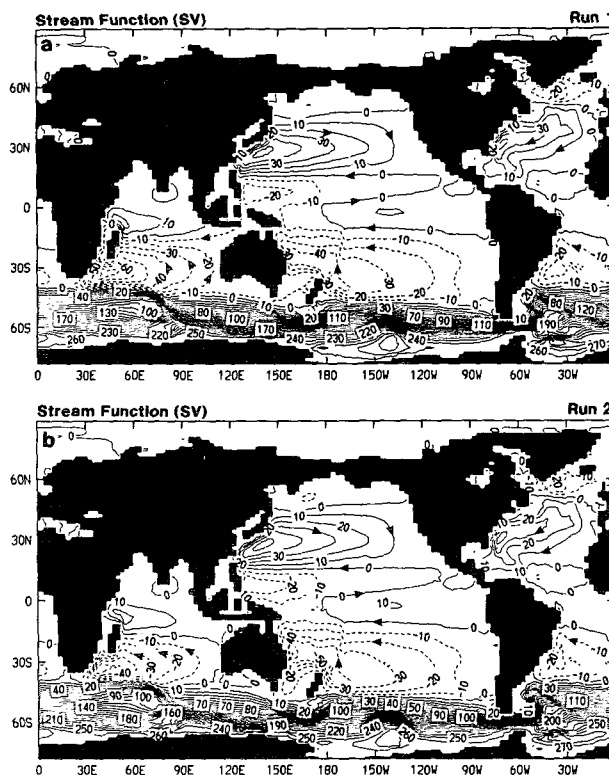


FIG. 5. Streamfunction of depth-integrated current for (a) run 1 and (b) run 2 (units: Sv). Arrow heads indicate flow direction.

flows inferred from Fig. 6 are very close to the actual model flows at levels 2–4. The top-level flow is somewhat modified by Ekman drift (e.g., compare Fig. 6a with Fig. 8a).

Streamfunctions for the meridional overturning circulation are shown in Fig. 7 for (a) the Atlantic, (b) the Indian–Pacific, and (c) the world oceans, for run 1. Most features are broadly similar to those found in other global ocean models (e.g., Semtner and Chervin 1988; Toggweiler et al. 1989). Formation and southward outflow of North Atlantic Deep Water is clearly evident in Fig. 7a. In contrast, the Indian and Pacific basins both features northward inflow of deep water and general upwelling.

2) INDIAN OCEAN

We turn now to the model climatology for the Indian Ocean. Note the general similarity between the pattern of depth-integrated (primarily wind driven) flow and the surface pressure (Figs. 5, 6). The single major exception occurs in a region from western Australia to southern Madagascar. There, the near-surface geostrophic flow is directed east/southeastward, opposite to the depth-integrated flow (indicating buoyancy-flux effects). This near-surface flow feeds a Leeuwin Cur-

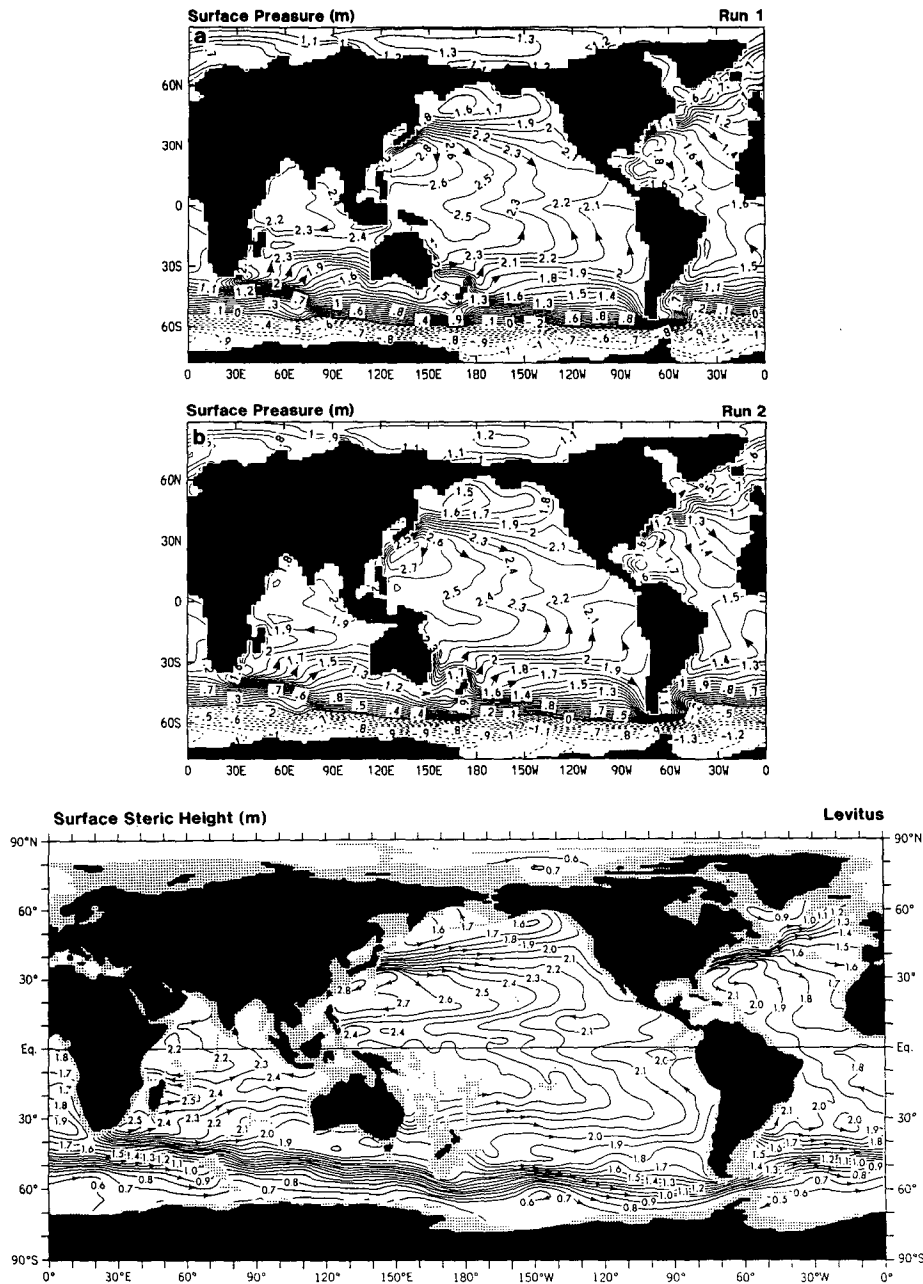


FIG. 6. Surface pressure fields for (a) run 1 and (b) run 2, and (c) surface steric height from Levitus (1982). Units are meters; surface pressure in (a) and (b) has been divided by $g\rho_0 (=10^4 \text{ kg m}^{-2} \text{ s}^{-2})$. Arrow heads indicate geostrophic flow direction. The global arbitrary constant has been set to ensure a maximum of 2.9 m in each case.

rent-like feature off western Australia. In both runs, the onshore-directed component of geostrophic flow exceeds that of the westward Ekman drift. The inflow sinks at the coast and returns towards the northwest in a Leeuwin Undercurrent (Fig. 8b, 9b). The whole pattern of southeastward geostrophic flow and southward coastal flow near the surface, coastal downwelling,

and a northwestward return flow at depth, will be referred to as the "Leeuwin Current system."

The remaining essential features of the near-surface circulation are shown in Figs. 8 (for run 1) and 9 (for run 2). Note the banded pattern of surface heat flux across the South Indian Ocean (Figs. 8c, 9c). The first, more intense, band of surface heat loss (centered at

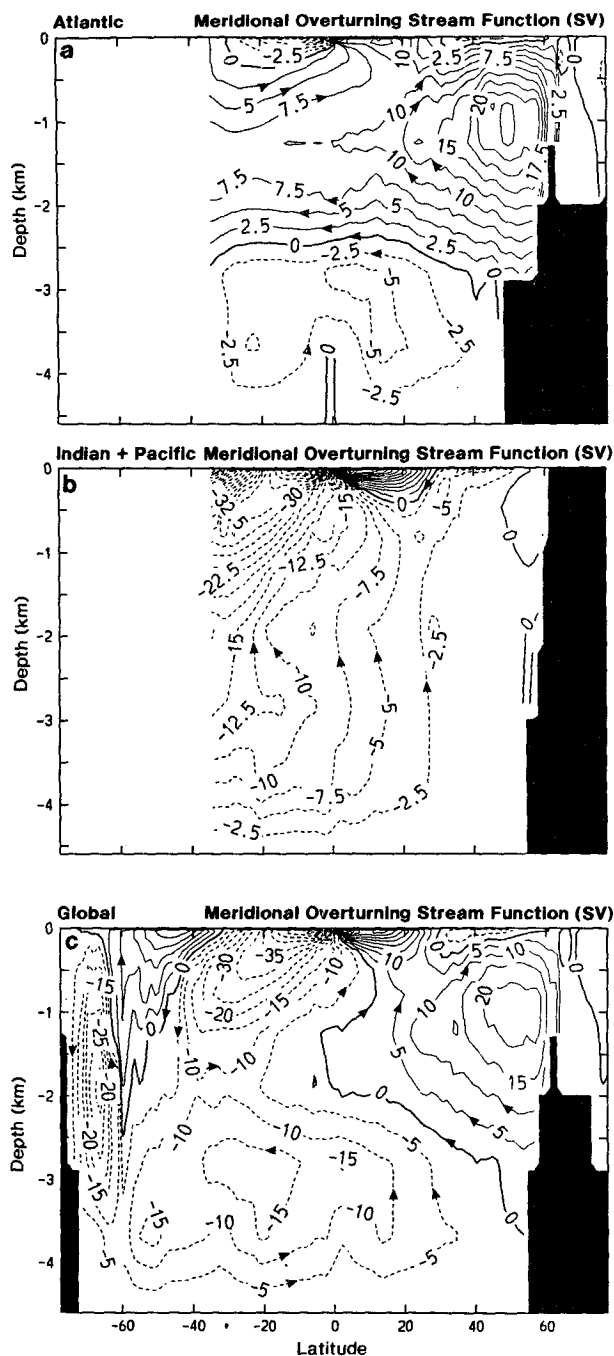


FIG. 7. Meridional overturning streamfunction for (a) Atlantic, (b) Indian-Pacific, and (c) world oceans, for run 1 (units: Sv). Arrow heads indicate flow direction.

about 40°S) corresponds to the warm water of the Agulhas retroflection and outflow (Fig. 10e). The second band of heat loss is associated with southward Ekman drift between 15° and 25°S; in the east it intensifies and extends all the way down the western Australian coast (especially in run 1). This extension

corresponds to the warm water associated with the southeastward near-surface flow mentioned above. These bands of surface heat loss are characterized by convective mixed layers that deepen progressively along the path of the flow (Figs. 8d, 9d), as the mixed-layer water cools (Fig. 9e). The model mixed layers are typically about a factor of 2 too deep, compared to observations (e.g., Colborn 1975; Levitus 1982, Fig. 96a); however, the patterns of progressive deepening along the above flow features appear realistic. The excessive depth of convection appears linked, at least in part, to the general weakness of the upper density structure. Convective mixing will be seen to strongly modulate the pattern of surface heat flux response to the Indonesian throughflow.

3) SOUTH PACIFIC OCEAN

The circulation of the model South Pacific partly resembles that of the Indian Ocean. The single major exception is that the eastward geostrophic flow turns northward in the subtropical east Pacific to feed the equatorial upwelling, rather than continue on to the eastern boundary. Consequently, the onshore component of geostrophic flow is weak and is offset by offshore Ekman drift in the top level; thus, coastal upwelling results along the subtropical South American coast. However, south of about 40°S, the eastward geostrophic flow in the Pacific does recurve southeastward as it approaches the South American coast. Downwelling occurs at the coast and a deep undercurrent develops that flows towards the north/northwest (Fig. 10a). The pattern here is in many ways analogous to the Leeuwin Current System of the eastern Indian Ocean.

As in the Indian Ocean, the surface heat flux field in the South Pacific displays a banded pattern (Fig. 1a). One prominent band of surface heat loss runs almost due east from New Zealand to near Cape Horn; it initially corresponds to the outflow of the East Australian Current (EAC). Another band of weak surface heat loss is found between 18°S and 28°S in the west and central Pacific, where it is associated with southward Ekman drift. This band curves southeastward and strengthens in the eastern Pacific, where it becomes associated with the south/southeastward geostrophic flow near the southern South American coast. Convective mixed layers again form along both bands (Fig. 10b). These bands are analogous to the two bands of surface heat loss in the Indian Ocean. Farther north, there is an equatorial band of very strong heat gain, associated with wind-forced (Ekman) upwelling.

4) EAST INDIAN VERSUS WEST PACIFIC OCEANS

The throughflow will act to reduce water property differences between the western Pacific and eastern Indian oceans. Water mass differences across the Indonesian isthmus in run 2 are shown in Table 3, for

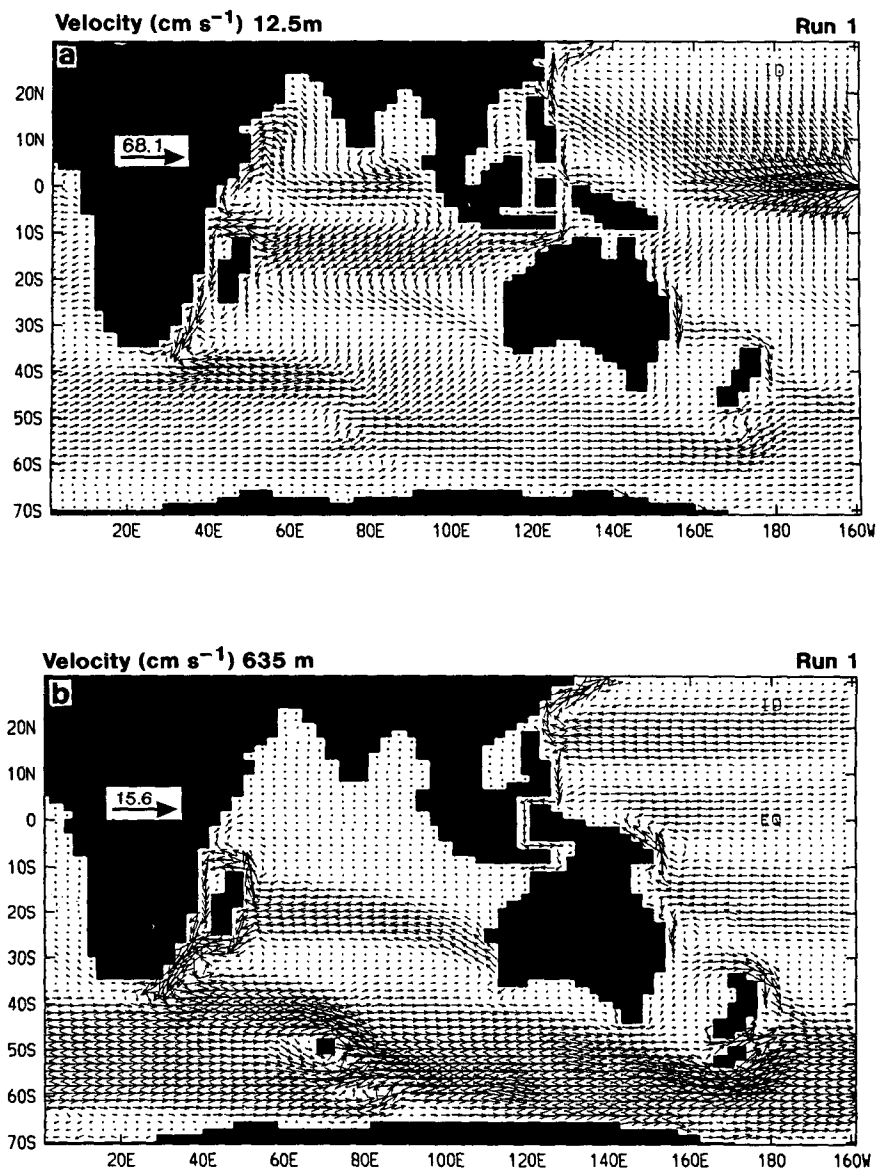


FIG. 8. Total fields for run 1, in the Indian/southwest Pacific region: (a) velocity at 12.5 m (cm s^{-1}), (b) velocity at 635 m (cm s^{-1}), (c) surface heat flux (W m^{-2}), (d) deepest level reached by convection from surface. Note different velocity scales on (a) and (b).

area A minus area B . Area A (0° – 10°N , 125° – 134°E) represents the Mindanao source region of throughflow water in the passage-open cases; area B (10° – 16°S , 108° – 122°E) represents the throughflow exit region. When the oceans are separated, water above 500 m on the Pacific side of the Indonesian isthmus is much less dense than on the Indian Ocean side (it is fresher and much warmer). The density differences are much reduced in the passage-open cases (Table 3). These changes in density between the runs incite extensive baroclinic responses in both oceans, as documented later in section 4b.

b. Full throughflow versus no throughflow

In this section the solution of the full throughflow case (run 1) is compared with that of the no throughflow case (run 2). We begin by examining the effect of the throughflow on the depth-integrated flow field. The pattern of response for this field is easily interpreted in terms of viscous dynamics and has significant consequences for the upper-ocean temperature response. The details of the thermal response and consequences for the surface heat flux are then considered for each ocean basin individually.

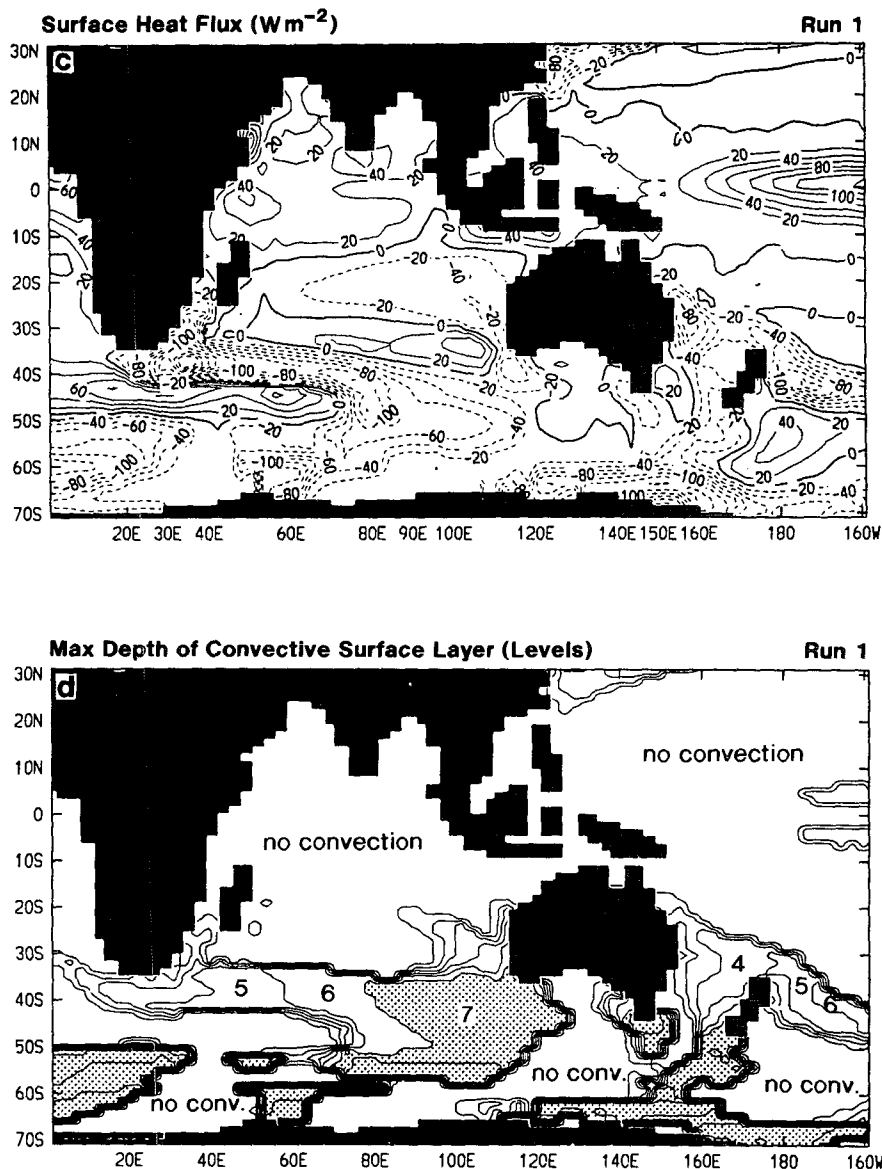


FIG. 8. (Continued)

1) RESPONSE OF DEPTH-INTEGRATED FLOW

On comparing Figs. 5a and 5b, we see that run 1 features a stronger Indian South Equatorial Current (SEC) and Agulhas Current, and a weaker EAC than does run 2. These perturbations are seen more clearly in Fig. 11a, which shows the run 1 minus run 2 difference in the streamfunction of depth-integrated flow (ψ'). An Indian Ocean/South Atlantic/east Australian coast circuit is clearly evident. Effects on the depth-integrated flow elsewhere in the World Ocean are negligible (except for the perturbation eddy south of New Zealand).

Most aspects of the perturbation flow in Fig. 11a are very similar to those expected from a simple Sverdrup model (Godfrey 1989) shown in Fig. 11b. There are some significant exceptions, including partial reflection south of Africa and the development of recirculations east of southern Africa and Australia (which considerably enhance the impact of the Indonesian throughflow on local current strengths). Terms that can contribute to deviations from Sverdrup flow include bottom stress [Eq. (1)], momentum advection, lateral viscosity, and bottom topographic effects. However, the bottom stress and momentum advection terms are typically one to two orders of magnitude less

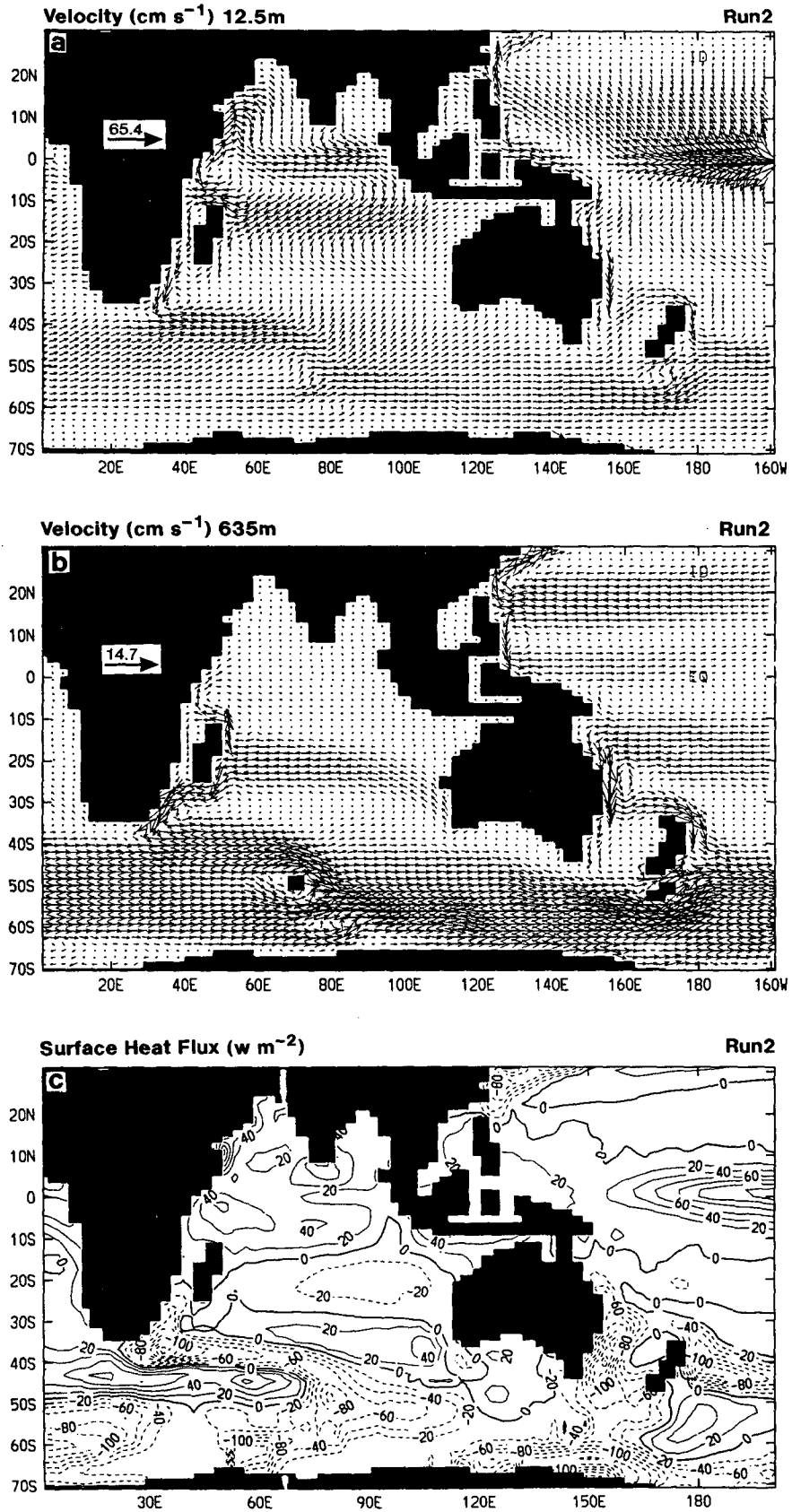


FIG. 9. Total fields for run 2, otherwise as for Fig. 9 except that (e) SST ($^{\circ}\text{C}$) is also shown.

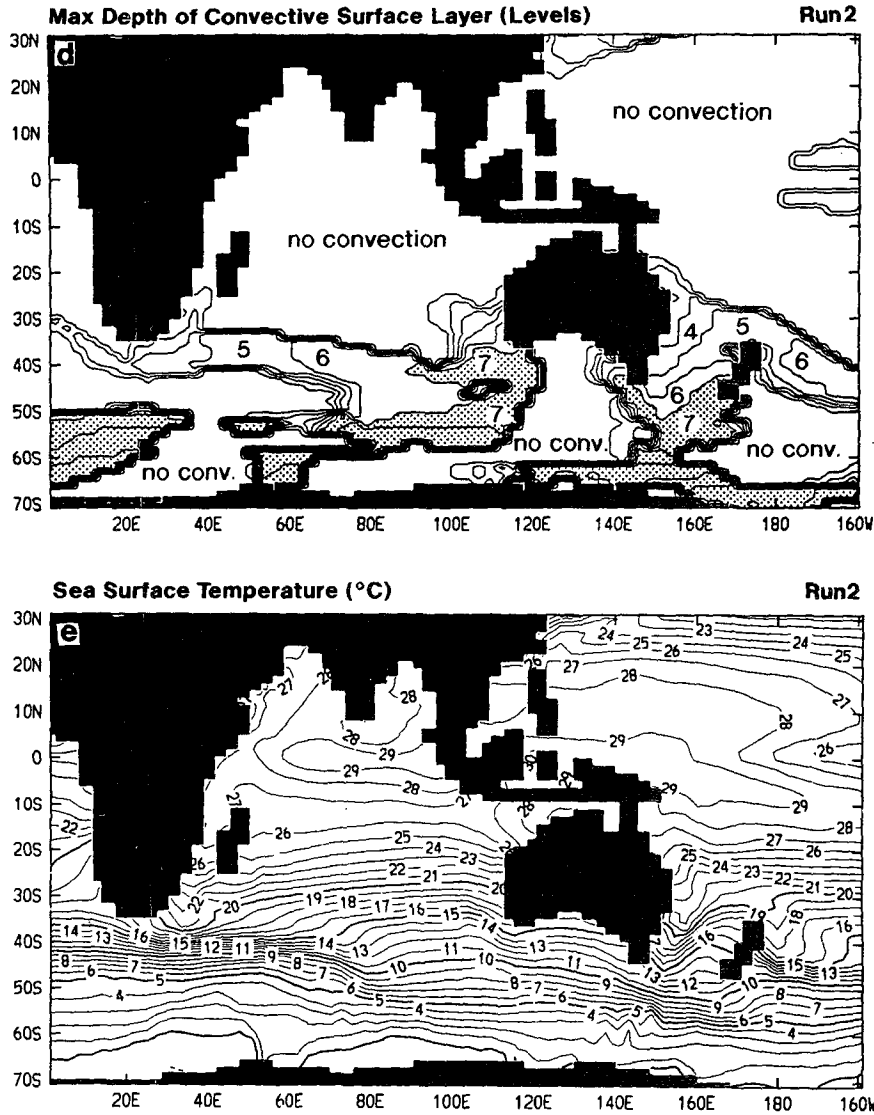


FIG. 9. (Continued)

than the lateral viscous terms, in the present model. (The negligible effect of the former terms was verified by a direct model experiment, which involved a repeat of run 1 stage 2 but with these terms eliminated.) Thus, bottom topography and lateral viscous effects are the only likely mechanisms for the non-Sverdrupian aspects of Fig. 11a.

It is, therefore, likely that away from major subsurface topographic features ψ' can be modeled reasonably well by the simple Munk (1950) viscous model; that is,

$$-\beta\psi'_x + A_{MH}\nabla^4\psi' = 0, \quad (5)$$

where ∇^4 is the biharmonic operator. To test this simple model, we solved Eq. (5) via a Jacobi iteration using centered finite differencing on a grid corresponding to

the full model between 60°N and 70°S. Continental boundaries are taken to be isopleths at the 800-m depth; however, a perturbation flow is allowed through an Indonesian passage. Drake Passage is closed and the small islands are either neglected or merged with the larger land masses. The boundary conditions are (i) $\psi' = 0$ over Africa/Eurasia/America/Antarctica, (ii) $\psi' = -17.1$ Sv over Australia/New Guinea, and (iii) $\psi'_x = \psi'_y = 0$ at the coastlines. The standard value of A_{MH} (Table 2) is used and β is simply assigned the constant value $1.87 \times 10^{-11} \text{ m}^{-1} \text{ s}^{-1}$. The resulting perturbation streamfunction is shown in Fig. 11c. The simple model captures most features seen in Fig. 11a. The coastal boundary flows are well represented. The non-Sverdrupian recirculations to the east of the boundary currents are also evident, though they are

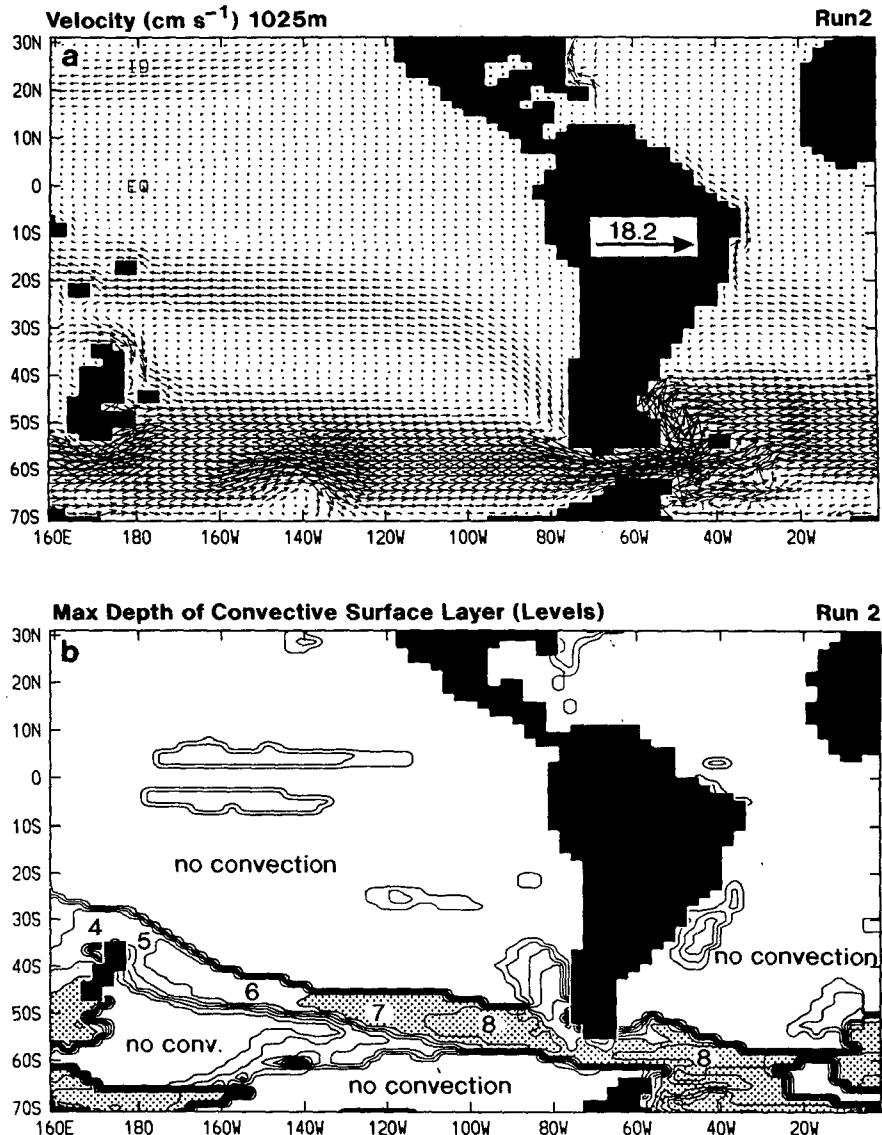


FIG. 10. Total fields for run 2 in the South Pacific/southwest Atlantic region: (a) velocity at 1025 m (cm s⁻¹), (b) deepest level reached by convection from surface.

not as strong as in the full model. Additional very weak recirculations of alternating sign, evident in the Pacific in Fig. 11c (but not in Fig. 11a), correspond to the damped sinusoids discussed by Munk (1950). The partial retroflection south of Africa is present in Fig. 11c. The westward weakening of the South Atlantic branch is also apparent; however, this branch is less diffuse than in Fig. 11a.

2) THERMAL CONSEQUENCES OF DEPTH-INTEGRATED FLOW

Godfrey (1989) assumed that perturbation flows like those shown in Figs. 11a or 11b are confined to depths above major topographic features. If so, then the requirement that these flows be balanced by the thermal

wind implies large changes in the density fields between the runs. Godfrey suggested that these changes would primarily be effected by temperature changes, with potential implications for the surface heat flux.

Specifically, a zonal jet of transport V at latitude y requires a depth-integrated difference in pressure ΔP across the jet of $\rho_0 f(y)V$ [where ρ_0 is the water density and $f(y)$ the Coriolis parameter]. If all flow occurs above a certain depth Z , then pressure gradients equal $\rho_0 g$ times gradients of steric (i.e., dynamic) height, relative to a depth of no motion at Z . Thus, the depth-integrated difference in steric height ΔH across the jet is given by

$$\Delta H = \frac{f}{g} V. \quad (6)$$

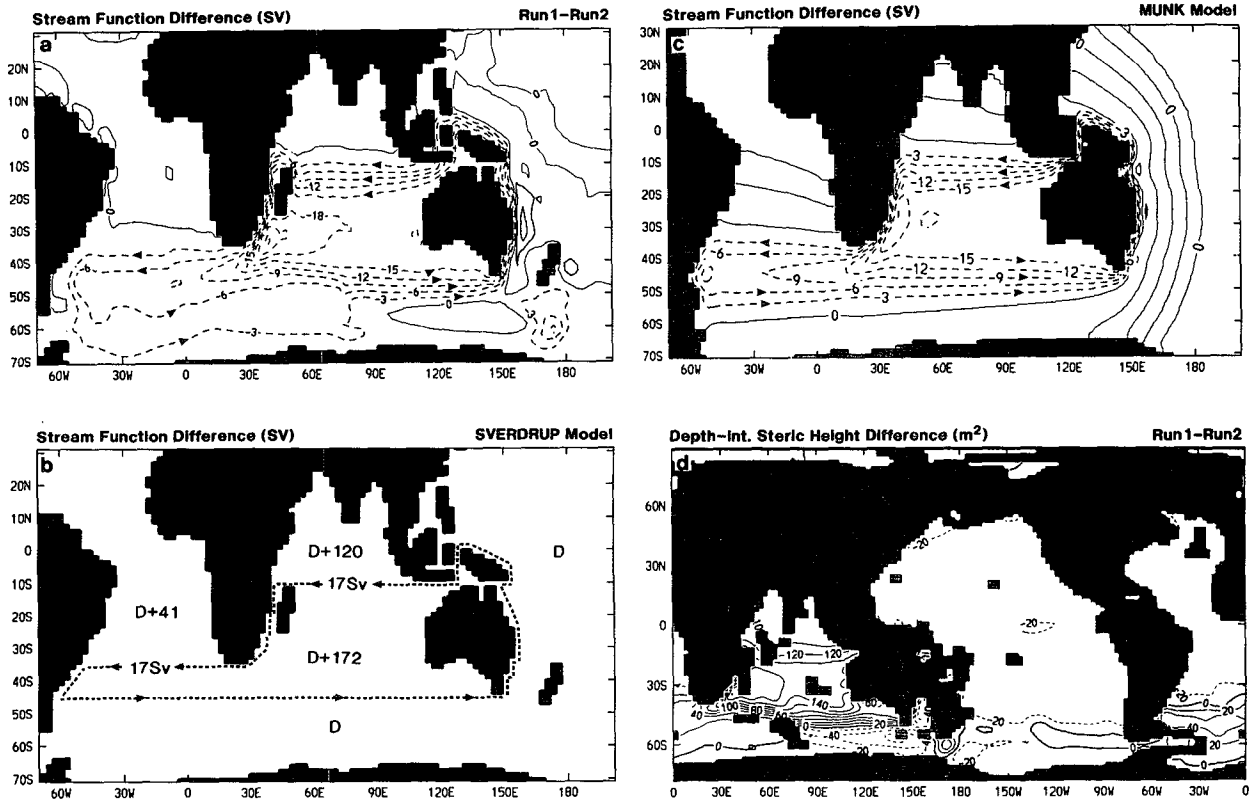


FIG. 11. Streamfunction difference for run 1 minus run 2: (a) for full model, (b) expected from Sverdrup model, and (c) expected from Munk (1950) viscous model (units: Sv). Also, (d) depth-integrated steric height difference, over depths 0 to 2800 m; units are square meters. Numbers in Fig. 11b indicate implied differences in depth-integrated steric height (in m^2).

In the Boussinesq approximation, the steric height difference across the jet is ρ_0 times the depth integral of the specific volume-anomaly difference ($\Delta\delta$), so ΔH is the double depth integral of $\Delta\delta$ (e.g., Godfrey 1989). One of the integrals can be performed, yielding

$$\begin{aligned} \Delta H &= \rho_0 \int_Z^0 z \Delta\delta(z) dz \\ &= \int_Z^0 z \alpha(z) \Delta T(z) dz, \end{aligned} \quad (7)$$

where the second equality holds if salinity effects can be neglected. Here $\Delta T(z)$ is the temperature difference across the jet and $\alpha(z)$ the thermal expansion coefficient at depth z . We can use (7) to define a depth-weighted mean temperature difference ΔT_m via

$$\Delta H = \alpha' Z^2 \Delta T_m / 2, \quad (8)$$

where α' is a mean value of the thermal expansion coefficient.

If Godfrey's assumptions are valid, the relations (6) and (8) may be used to relate changes in the transport streamfunction to changes in depth-integrated steric height H' and weighted-mean temperature T'_m . A

physical appreciation is gained by noting that the depth-integrated difference of steric height is actually the difference in potential energies of the water column. Changes in the effective transport streamfunction may then be seen to be associated with raising or lowering the center of mass of the water column.

In the present case, (6) and (8) imply global-scale changes in H' and T'_m as a result of opening the Indonesian passage. At least in the simple Sverdrup case, the field of H' is readily calculated, within a global additive constant, via (6). If $V = 17 \text{ Sv}$ is the transport of the zonal jets in Fig. 11b, then the result of opening the Indonesian passage is to create a difference $\Delta H' = f(44^\circ\text{S}) \times 17 \text{ Sv}/g = 172 \text{ m}^2$ across the jet at 44°S and a difference of $f(12^\circ\text{S}) \times 17 \text{ Sv}/g = 52 \text{ m}^2$ of opposite sign across the jet at 12°S . Similar considerations apply in the Atlantic. Thus, if H' has the value of D in the Pacific and Southern oceans, then we expect the changes in H' elsewhere to be as shown in Fig. 11b. For reasonable values of Z and α' (1500 m and $2 \times 10^{-4} \text{ K}^{-1}$) Eq. (8) implies that the South Indian Ocean warms by 0.8°C relative to the Pacific, in a depth-weighted-mean sense, as a result of opening the Indonesian passage. The North Indian Ocean must also warm by 0.5°C , and the Atlantic by 0.1°C , relative to the Pacific.

which accounts for about two-thirds of the average perturbation heat loss in that region (Fig. 14c).

and the generally stronger temperature perturbation surface velocity (Fig. 14a). In contrast, tem-

Godfrey's assumption that the flow is confined to the upper part of the ocean is reasonably valid in our model. Difference currents are quite weak below about 1500 m (e.g., Fig. 12c); in particular, perturbation flows below 2800 m are very weak and disorganized. Figure 11d shows the actual difference in depth-integrated steric height relative to 2800 m between the two runs. The mean value of H' in the Pacific and Southern oceans is roughly $-30 \text{ m}^2 (=D)$, while it is about 160 m^2 in the southern Indian Ocean and 90 m^2 in the northern. The differences are quite similar to the expectations in Fig. 11b. However, H' in the Pacific and Atlantic are very similar, unlike Fig. 11b. This discrepancy is partly because the Sverdrup approximation is poor south of the Atlantic. Nevertheless, the broad prediction of the existence of global-scale changes in H' is well satisfied.

3) INDIAN OCEAN THERMAL RESPONSE

The relationship between temperature changes and the perturbation currents is illustrated in Fig. 12, which show sections of (a) potential temperature, (b) salinity, and (c) zonal velocity differences (run 1–run 2) along 90°E . The warming of the Indian Ocean implied by Figs. 11a and 11d is clearly evident in Fig. 12a. Only very small temperature changes are found south of 50°S , while large subsurface warming occurs at all latitudes farther north. The salinity differences (Fig. 12b) are generally small enough to have a relatively small effect on density.

It is convenient to divide the portion experiencing warming into four "regions." The first region (50°S –

37°S) features large temperature perturbations (T') extending from 1250-m depth to the surface. The second region (37°S – 28°S) is characterized by a deep T' maximum. The third region (28°S – 8°S) features shallower T' and S' maxima and strong vertical shear in the perturbation velocity fields (Fig. 12c). The fourth region (8°S – 20°N) features a uniform T' profile with a maximum around 300-m depth. Overall, the depth of maximum T' is least in the tropics; it roughly follows the main thermocline that broadly rises toward the equator (Fig. 12d). Yet, it is only at the higher latitudes (50°S – 37°S) that large temperature perturbations reach the surface, thereby allowing a large perturbation heat loss to the atmosphere.

The meridional structure evident in Figs. 12a–c is typical of the response over much of the Indian Ocean. Figure 13 shows T' at (a) 370-m and (b) 1025-m depth. The basinwide subsurface warming is clearly evident. The largest T' values are seen near the west Australian coast and are associated with strongly enhanced coastal downwelling. The extensive warming seen over the remainder of the basin is maintained against diffusive erosion partly by weakly enhanced subtropical downwelling and partly by enhanced horizontal advection in the Agulhas Current/outflow and in flows stemming from the Australian coastal downwelling.

Figure 14 shows run 1 minus run 2 difference fields of (a) top-level velocity, (b) velocity at 635 m, (c) surface heat flux, and (d) SST, for the Indian–southwest Pacific sector. The first region noted above (over 50° – 37°S) is seen in Figs. 14c,d to be part of an extensive band of higher SST and surface heat loss, which extends east–west across the Indian Ocean sector. This band

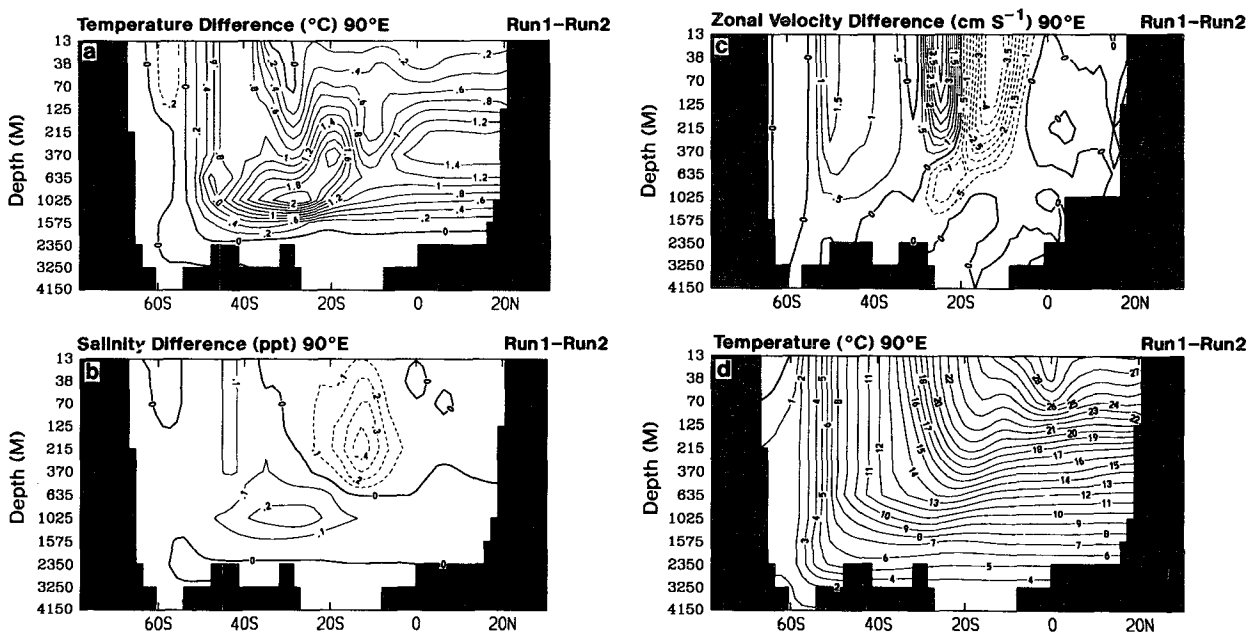


FIG. 12. Meridional-depth sections of difference fields at 90°E for run 1 minus run 2: (a) temperature ($^\circ\text{C}$), (b) salinity (psu), (c) zonal velocity (cm s^{-1}). Also, (d) total temperature field for run 2 ($^\circ\text{C}$).

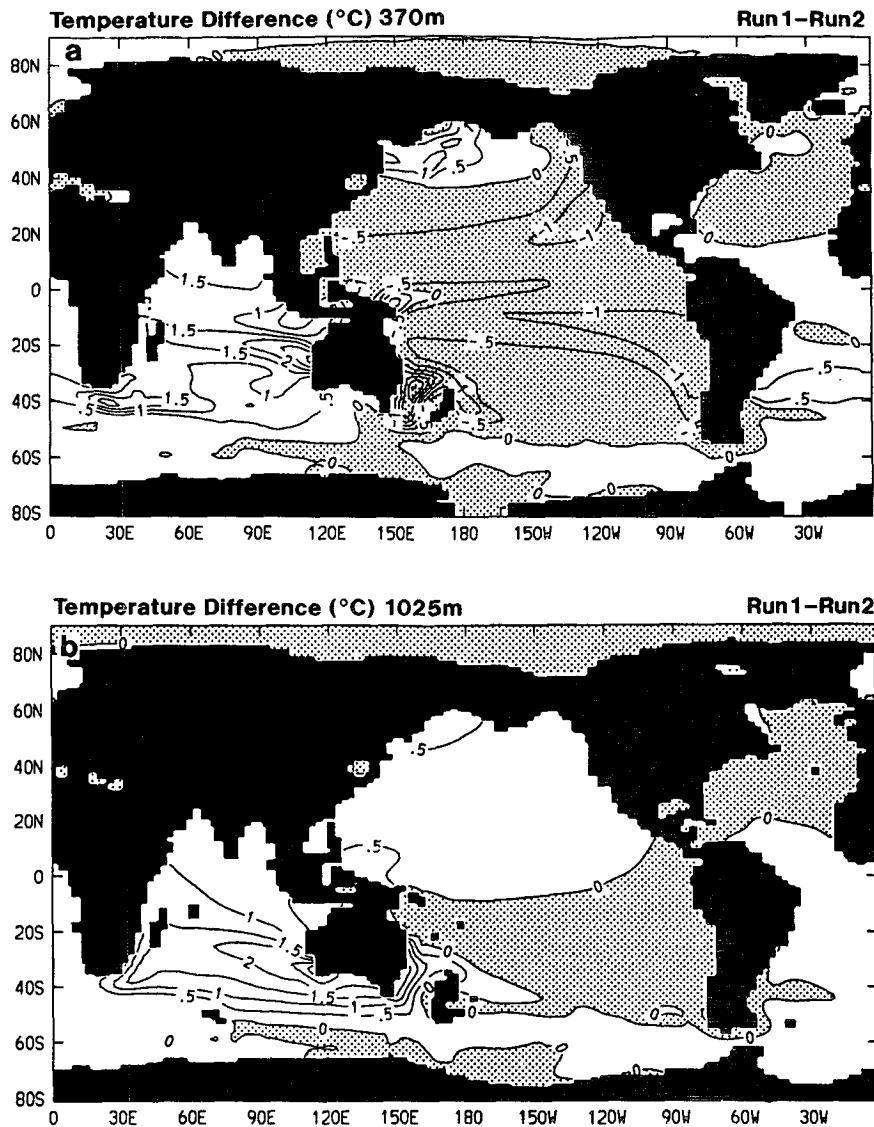


FIG. 13. Temperature differences for run 1 minus run 2 at (a) 370 m and (b) 1025 m (units: °C). Negative values are shaded.

corresponds to the region of convective mixing associated with the Agulhas outflow (Figs. 8d, 9d). The convective mixing allows for efficient communication between the surface layer and deeper water, so that a subsurface warming almost immediately leads to surface warming and thus enhanced surface heat loss.

The other three regions are not subject to convective mixing at 90°E. There, subsurface warming may be communicated upward only by vertical motion or vertical diffusion. Both are relatively inefficient mechanisms, and SST perturbations are small. For example, in region 4, the vertical T' gradient in the top 210 m is about $1.4^\circ\text{C}/210\text{ m}$ (Fig. 12a). This gradient implies a mere diffusive heat flux of $\rho_0 C_w A_{TV} \partial T' / \partial z = 2.7\text{ W m}^{-2}$, which accounts for about two-thirds of the average perturbation heat loss in that region (Fig. 14c).

Elsewhere, shallow, Ekman-induced upwelling near 8°S and along the Somali coast make but minor (less than $+3\text{ W m}^{-2}$) contributions to the perturbation upward heat transport at those locations.

The small surface response outside regions of convective mixing is related to the lack of a mechanism to generate large SST perturbations in the face of the surface restoration. Enhanced surface advection accounts for up to $+15\text{ W m}^{-2}$ of the perturbation surface heat loss in the throughflow exit region (between Australia and Java) but is mostly small elsewhere (Fig. 16a). The overall weakness and limited extent of changes in surface horizontal advection result from the small heat capacity of the thin (25-m deep) surface layer and the generally small magnitude of the perturbation surface velocity (Fig. 14a). In contrast, tem-

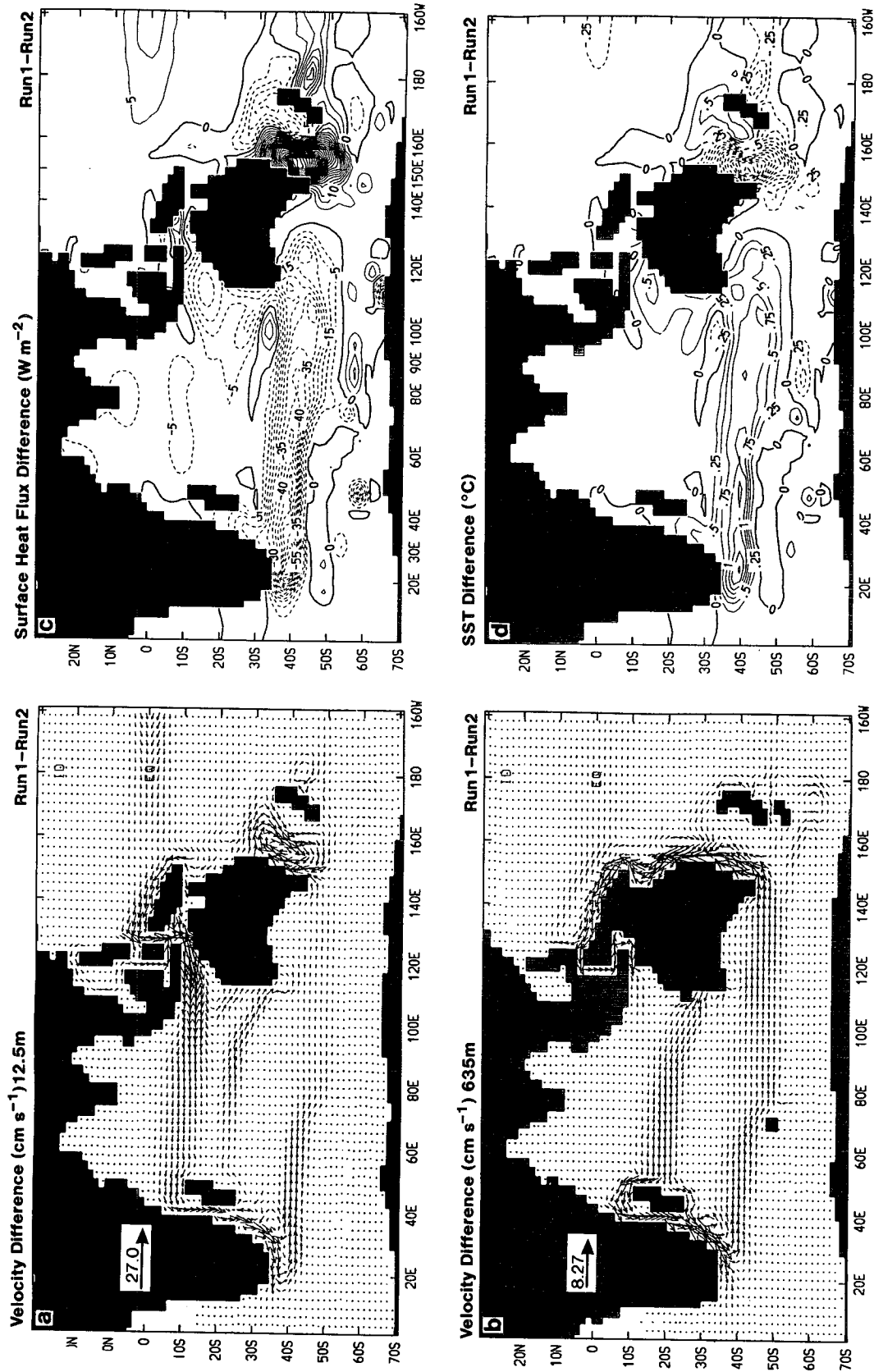


FIG. 14. Difference fields for run 1 minus run 2, in the Indian/southwest Pacific region: (a) velocity at 12.5 m (cm s^{-1}), (b) velocity at 635 m (cm s^{-1}), (c) surface heat flux (W m^{-2}), and (d) SST ($^{\circ}\text{C}$). Note different velocity scales on (a) and (b).

perature perturbations at depth are largely insulated from the surface restoration and may extend great distances via either direct advection or baroclinic wave propagation. The subsurface heat is released upon encounter with a convective mixed layer, which may be far removed from the source.

Region 3 (28°S–8°S at 90°E) deserves further attention. The northern portion features the rather shallow current stemming from the throughflow. The southern portion is dominated by a strong secondary flow feature, namely, an eastward surface jet with a westward flow of roughly equal transport beneath it (note the very nonlinear depth scales in Fig. 12). The equality of flow is required to satisfy the constraint of zero depth-integrated flow at these latitudes [section 4b(1)]. The surface flow/underflow pair is clearly evident in Figs. 14a,b and extends across the Indian Ocean. In fact, this feature simply represents an enhancement of the surface flow/underflow pair associated with the weak Leeuwin Current system of run 2 (Figs. 7b, 9a,b). Other features of the Leeuwin Current system are also enhanced in run 1 over run 2, including area and depth of convection off western Australia (Figs. 8d, 9d), surface heat loss (Fig. 14c), and coastal downwelling as mentioned earlier. Thus, the throughflow has the effect of strengthening the entire Leeuwin Current system, *in situ*.

The surface flow/underflow pair noted above is an analog of the broad zonal flow and underflow found by GW and HWG in their warm Pacific runs. In GW, the flows extend westward across the Indian Ocean basin. In HWG, where a wind-forced Sverdrup circulation is included, the flows arc northwest then west in a pattern rather similar to that in Figs. 14a,b. The curved path followed by these flows resembles that for the solution characteristics calculated by Luyten and Stommel (1986) in the "eastern regime" of their two-layer model of the subtropical gyre. These characteristics stem from the eastern ocean boundary, and their orientation is governed by the (westward) propagation velocity of nondispersive internal Rossby waves as modified by the Sverdrup transport vertically averaged over the active ocean layers. The characteristics are initially directed equatorward and westward, under the influence of the equatorward Sverdrup transport in the eastern basin.

In the present model, west Pacific warm water sets the density profile at the equatorward end of the Western Australian coast in run 1, resulting in a substantial density decrease there over that in run 2. Presumably, internal-mode coastal Kelvin waves attempt to transmit this density decrease southward along the coast, where enhanced convective heat loss acts to progressively mitigate the density decrease in the upper layers. The result is an enhancement of the longshore steric height gradients (Fig. 6), onshore geostrophic flow near the surface, and coastal downwelling. Away from the coastal convective zone, the diffusive buoyancy flux is

rather small. Under such circumstances, a model of the Luyten–Stommel type would be expected to show extension of the altered pattern of coastal density along the characteristics into the ocean interior. Perturbation flow would then develop (via the thermal wind relation), which approximately follows the characteristics.

The surface heat flux perturbations in Fig. 14c are broadly consistent with the results of HWG (warm versus cold west Pacific) off western Australia. They found changes there of up to 60 W m^{-2} compared to the 20 W m^{-2} seen in Fig. 14c, but this is presumably due to their stronger difference in thermal forcing. However, the present intense response in the Agulhas Outflow contrasts with HWG, who find a mere $10\text{--}30 \text{ W m}^{-2}$ change there. This discrepancy may be related to the lack of change in their Agulhas Current strength (cf. Fig. 14a,b), which in turn is linked to their zero net throughflow. The effect of purely baroclinic throughflow in our model is explored in section 4c.

Finally, we note that a (relatively weak) Leeuwin Current system persists in run 2 even though the passage is closed, whereas GW and HWG find no Leeuwin Current features in their "cold Pacific" cases. The most likely reason is that in the present run 2, the temperature profiles off Western Australia may be set by Kelvin waves radiating south from the Indonesian coast, and typical temperature profiles there are much warmer than those observed off Peru (used by GW and HWG to define their "cold Pacific" case).

4) PACIFIC OCEAN THERMAL RESPONSE

The loss of warm upper-level water to the Indian Ocean and the compensating inflow of colder water from the south produce a cooler Pacific in the full throughflow case (run 1). The surface heat flux response (Fig. 1b) shows perturbation surface heat gain over most of the Pacific, implying lower surface temperatures. Perturbation heat gain over most of the Pacific is small. In only a few regions are changes in the heat flux greater than 5 W m^{-2} .

By far the most intense thermal response is centered in the southwest Tasman Sea, where large negative temperature perturbations extend to 800-m depth (e.g., Figs. 13a, 14d). The intensity of the response appears linked to marked changes in the current structure of the Tasman Sea. The no-throughflow case features southward flow from the EAC that extends all the way to Tasmania (Fig. 9a,b). Warm water advected into the Tasman cools strongly (Fig. 9d). This is in contrast to the full throughflow solution (Figs. 8a,b), where the EAC totally separates from the coast at about 32°S, and weak northward flow is found at all levels 1–8 in the southwestern Tasman Sea. This flow advects colder water from the south, and there is weak surface heat gain over part of this region. Therefore, the intensity of thermal response in the southwestern Tasman Sea appears to result from a *reversal* of current direction

to considerable depth, between runs 2 and 1, and resulting replacement of warm EAC water by colder southern water. The current reversal is foreshadowed by comparison of the depth-integrated currents for the two runs (Figs. 5a,b). The Tasman Sea reversal stands in contrast to most of the other differences between the run 1 and run 2 solutions, where the throughflow simply acts to strengthen or weaken features of the run 2 solution, without changing their sign.

The intense temperature decrease of the upper Tasman Sea overlies a deeper temperature increase, which is partly connected to the Indian Ocean thermal response. At 370 m (Fig. 13a), the positive perturbation in the Indian Ocean appears eroded toward the east by convective cooling in the Agulhas outflow, so does not affect the Tasman Sea. At levels below the convection, the positive perturbation extends smoothly eastward into the Tasman Sea (Fig. 13b). This pattern indicates some recirculation of heat back into the Pacific from the Indian Ocean, though at depths too great to directly affect the surface heat flux.

Mixed-layer temperatures around northern New Zealand are higher in run 1 than run 2 and surface heat loss is enhanced (Fig. 14c). The higher temperatures appear to result from the more direct route of the EAC to this region in run 1. However, temperature perturbations beneath the convective mixed layer are negative (Fig. 13), and so the mixed layer T' changes sign as the layer deepens east of New Zealand.

Elsewhere in the Pacific, the opening of the Indonesian passage produces a systematic, basinwide baroclinic response. A brief description of this response is appropriate, since the associated subsurface temperature perturbations govern the surface heat flux pattern of Fig. 1b. Figure 15 shows the perturbation currents for the South Pacific at (a) the surface and (b) 1025-m depth. In the tropical western basin, the response is characterized by westward flow near the surface and eastward flow at depth (Figs. 15a,b). Farther east, these flows fan out to the north and south, in a pattern again reminiscent of Luyten and Stommel (1986) characteristics. The southern branch extends to Cape Horn. The northern branch (not shown) continues on, roughly following the coast of North America and eastern Siberia, such that there is a clockwise upper circulation and counterclockwise deep circulation all the way around the North Pacific from near northern Japan to the equatorial west Pacific. These flows are associated with the distinctive fan-shaped pattern of subsurface temperature change evident in Fig. 13a (NB, salinity effects dominate in the far North Pacific). Otherwise, weak positive density perturbations (mostly via negative T') are general north from 50°S, at depths less than about 1500 m.

As in the Indian Ocean, the surface temperature and heat flux fields are only strongly affected in regions where communication between subsurface and surface fields is enhanced. One such region is the central/east-

ern equatorial Pacific (Fig. 1b). This region coincides with the equatorial cold-water zone, characterized along the equator by strong Ekman-induced upwelling extending in the model to 160-m depth. The T' maximum occurs at 125–210 m near the equator, so the wind-forced motion facilitates upward advection of the subsurface T' . Figure 16 shows the contributions of (a) temperature advection (horizontal plus vertical) and (b) vertical diffusion (including convective mixing) to the perturbation heat budget for the surface layer. (Horizontal diffusion effects are negligible—the sum of the fields in Figs. 16a,b approximately equals the negative of the surface heat flux in Fig. 1b.) Advection dominates in much of the equatorial Pacific, while convective mixing dominates in most other regions.

Slightly enhanced surface heat gain also occurs in the upwelling zones along the North and South American coasts. Again, the small depth of the T' maximum assists transmission of the perturbation to the surface by advection and diffusion.

In the far south Pacific lie two bands of enhanced response, which coincide with the bands of surface heat loss and convective overturn noted in section 4a(3). Here the effect of the throughflow is to reduce the surface heat loss (cf. Indian Ocean convective regions). This is consistent with the negative subsurface temperature perturbations (Fig. 16a). Of particular interest is the band extending north/northwest from near Cape Horn, because it is associated with circulation features that correspond in many respects to the Leeuwin Current system of the Indian Ocean [section 4a(3)]. The total flow field shows south/southeastward flow overlying north/northwestward flow along this band (Figs. 6b, 10a). The perturbation flows (which form part of the large-scale Pacific baroclinic response) are directed exactly opposite to the total flows. Thus, the flow features in this region are weakened in the full throughflow case.

Finally, Fig. 1b shows a rather patchy response in the far North Pacific. All features in Fig. 1b in this region are associated with areas of convective overturn. The thin area of perturbation surface heat loss is associated with a slight northward shift of the front separating Kuroshio water from colder, fresher water farther north. This northward shift appears associated with the large-scale motions discussed above.

5) ATLANTIC OCEAN THERMAL RESPONSE

There are two routes via which the opening of the Indonesian passage may affect the Atlantic Ocean. One route is westward, around the southern terminus of Africa. The throughflow warms the Atlantic by this route (e.g., Fig. 14a). This warming results in part from increased “leakage” of Agulhas water into the Atlantic, from 1 Sv in run 2 to 3.5 Sv in run 1. The second route is eastward around Cape Horn, and the throughflow cools the Atlantic by this route. The negative T' in the

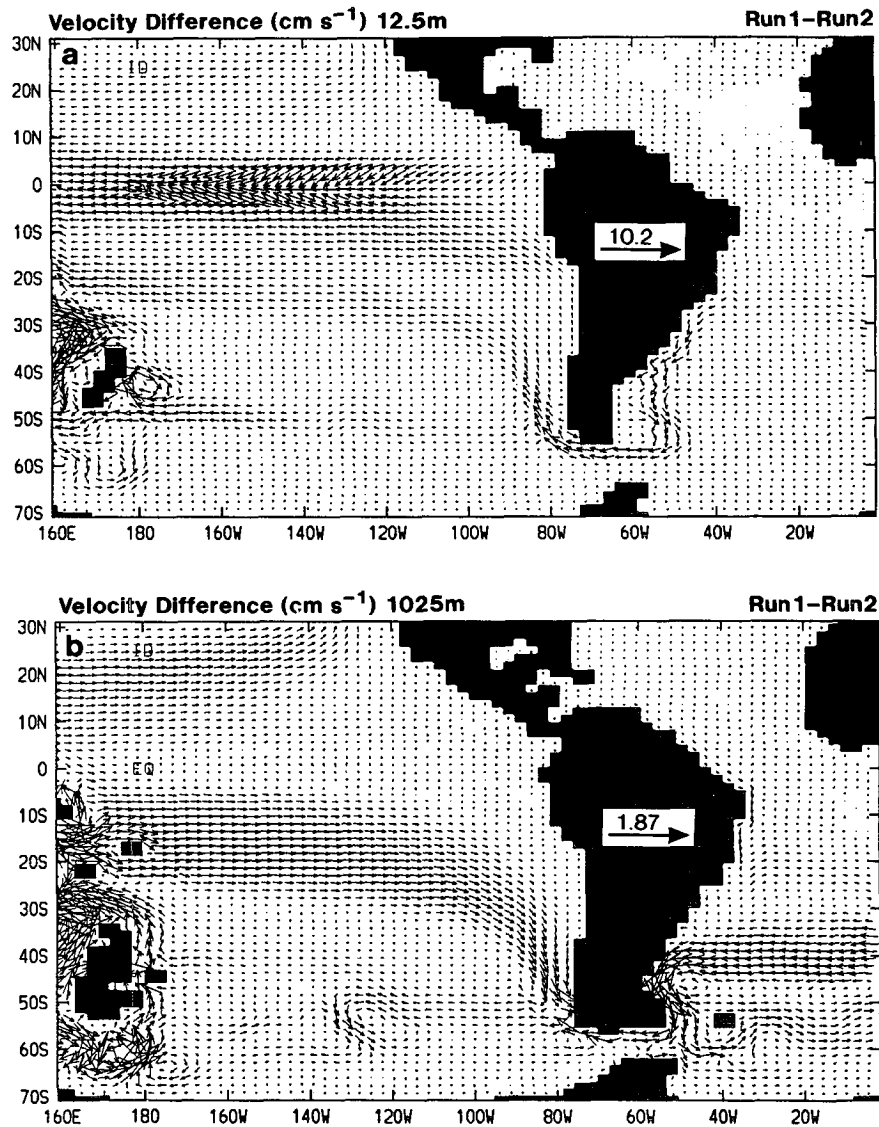


FIG. 15. Velocity differences for run 1 minus run 2, in the South Pacific/southwest Atlantic region at (a) 12.5 m and (b) 1025 m (units: cm s^{-1}). Note different velocity scales.

southeast Pacific is advected and/or propagates as per coastal Kelvin waves through Drake Passage and up the eastern South American coast. In the present model, the result appears to be an approximate cancellation of thermal effects over most of the Atlantic (Fig. 13), and surface heat flux changes are mostly very small (Fig. 1b). Salinity changes are also small in the North Atlantic, and North Atlantic Deep Water formation rates are little changed.

c. Baroclinic throughflow case

In the third model run, the net volume transport through the Indonesian passage is required to be zero; however, flow is permitted at any given depth. In the

following, we show the differences between our baroclinic throughflow (run 3) and no throughflow (run 2) cases, and compare these differences with those found by HWG. In both, the differences are forced by a change in buoyancy-induced flow through the Indonesian passages.

As expected, the streamfunctions for depth-integrated flow in our runs 2 and 3 are almost identical (to within 3 Sv). However, the velocity difference field for the surface (Fig. 17a) shows enhancements of the SEC and Leeuwin Current system that are only slightly smaller than in Fig. 14a. In addition, the near-surface Agulhas Current/outflow is slightly strengthened and the EAC very slightly weakened (cf. Fig. 14a). These surface difference flows are canceled by oppositely di-

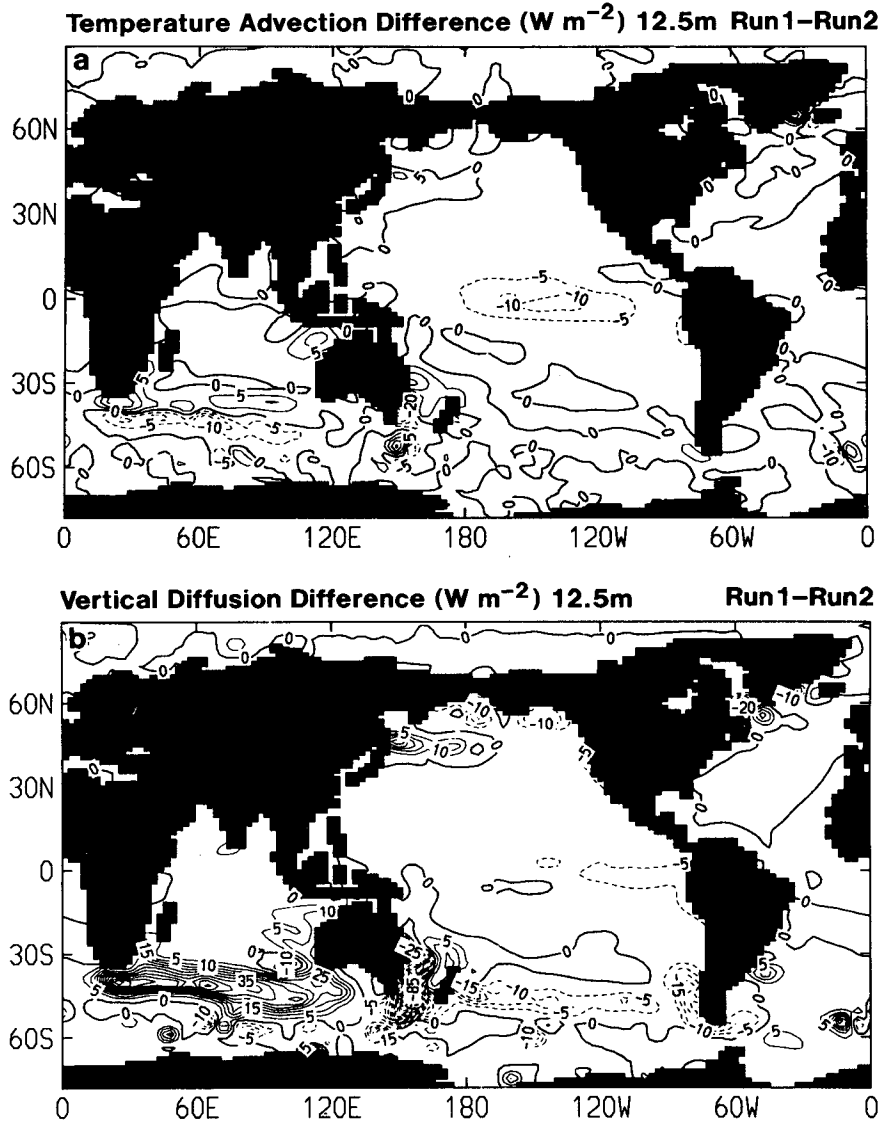


FIG. 16. Run 1 minus run 2 difference in rate of surface layer heating by (a) temperature advection and (b) vertical heat diffusion including convective mixing (units: $W m^{-2}$).

rected flows at depth. The reverse flows under the SEC and the Leeuwin Current inflow are strongest at 635 m (Fig. 17b). Here the Leeuwin Undercurrent hooks back underneath the SEC (cf. Fig. 14b). The Agulhas Current and EAC changes are canceled by flows at still greater depth (levels 8–10). Associated with all these flows are subsurface temperature perturbations, whose pattern at $90^{\circ}E$ broadly resembles that in Fig. 12a. The upper T' maximum at $20^{\circ}S$ is little diminished from Fig. 12a. The deep T' maximum of region 2 is much reduced, being about one-third that in Fig. 12a.

The difference in surface heat flux induced by the baroclinic throughflow is seen in Fig. 17c. The increase in heat loss off Western Australia is consistent with the enhancement of the Leeuwin Current system and is

little diminished from that for run 1–run 2 (Fig. 14c). Overall, the two difference patterns are very similar in the northern and eastern Indian Ocean. Furthermore, the patterns in the Agulhas Current/outflow and in the EAC regions are rather similar, though they are about three to six times weaker in the case of the baroclinic throughflow.

The heat losses in the Agulhas outflow are still comparable to those off Western Australia (Fig. 17c), in contrast to HGWs much weaker Agulhas outflow response. The principal reason for this discrepancy appears to be that convective mixed layers in their Agulhas Current and outflow are mostly very shallow, with strong stratification beneath, in their cold Pacific case. Strong subsurface warming occurs in their warm Pacific

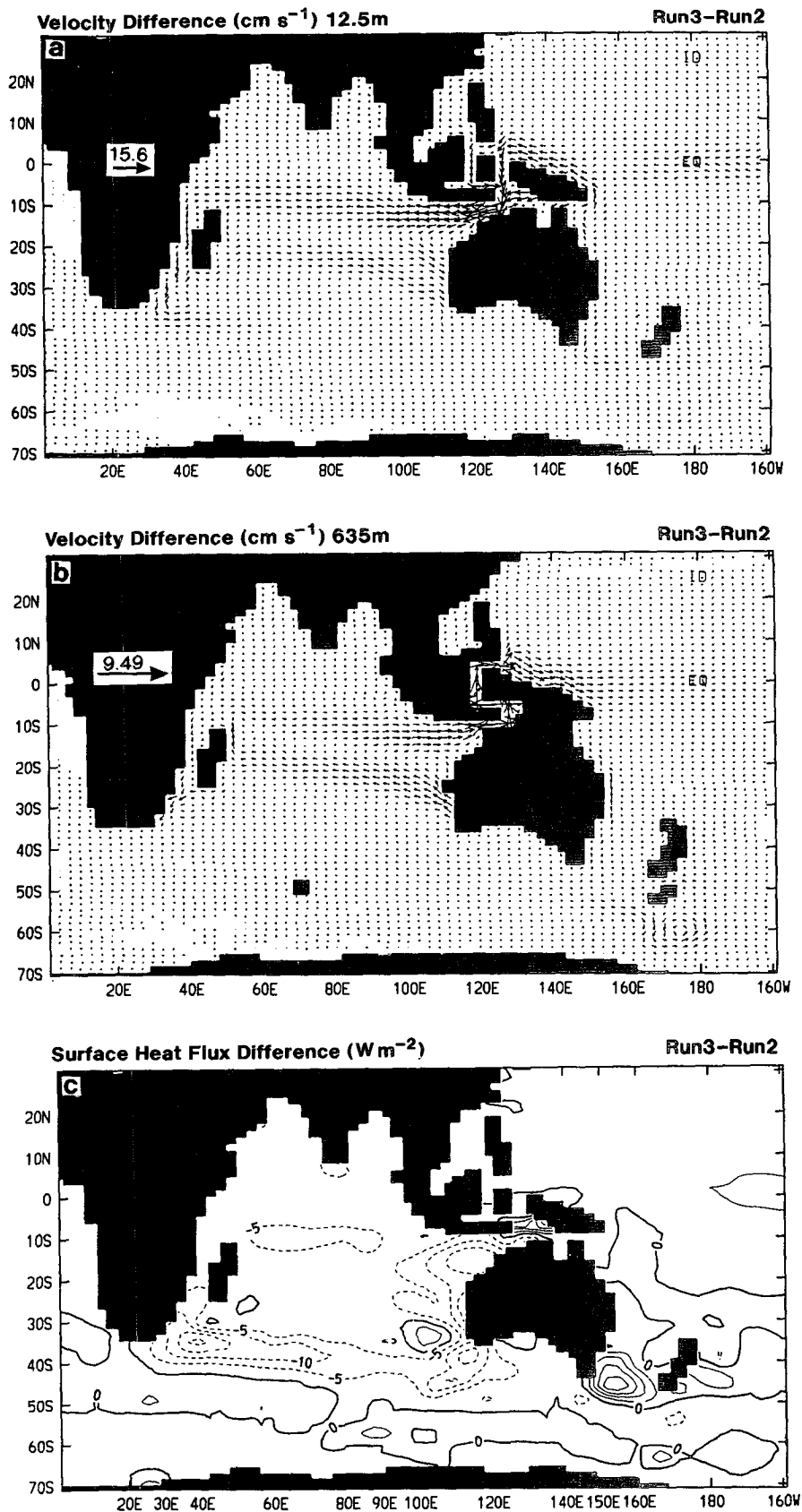


FIG. 17. Difference fields for run 3 minus run 2 in the Indian/southwest Pacific region: (a) velocity at 12.5 m (cm s^{-1}), (b) velocity at 635 m (cm s^{-1}), and (c) surface heat flux (W m^{-2}). Note different velocity scales on (a) and (b).

case (their Fig. 13a), but it is only by just enough to set off deeper convection, leaving mixed-layer temperature only slightly warmer. In our model, all runs have deep convective mixed layers in the Agulhas outflow, and subsurface warming is more fully expressed. In addition, HWG find essentially no enhancement of their Agulhas Current and outflow (cf. Fig. 17a). This is apparently because warm Kelvin waves propagating down the Australian west coast can then travel along their model's southern boundary. Flows associated with such waves would tend to offset any strengthening of the near-surface Agulhas Current and outflow. In our model, Kelvin waves would propagate northward up the east Australian coast and would act to reduce the EAC, instead of the Agulhas Current.

Another difference between our model and that of HWG is that our Indonesian sill is only 800 m deep, whereas they set a 1200-m deep sill. Manabe and Stouffer (1988) and Toggweiler et al. (1989), who also permit a pure baroclinic throughflow, set a sill depth of 1900 m. It is thus worthwhile to assess the effect of a deeper sill on the ocean circulation, in the case of baroclinic throughflow. To do this we conducted two additional model runs with only baroclinic throughflow permitted. In the first run (run 3b), the sill was lowered to 1250 m (on both sides of Sulawesi). In the second run (run 3c), all barriers in the Indonesian passages were lowered to 2800 m. Both runs were started from the final fields of run 3 and integrated for 60 000 steps (245/980 yr). The strength of the surface southward (and deep northward) flow through the Indonesian passages increases with sill depth, that is, 6.3 Sv for run 3, 9.1 Sv for run 3b, 11.8 Sv for run 3c. In run 3b, the Leeuwin Current system is further strengthened and surface heat loss increases to become almost identical to that of run 1 (to within a few $W m^{-2}$). Heat

loss from the Agulhas Current/outflow increases substantially, and run 3b minus run 2 differences are now *larger* there than in the Leeuwin Current region (cf. run 3 and HWG).

In run 3c, there is almost no further strengthening of the Leeuwin Current system, nor increase in heat loss from that region. The near equality of the Leeuwin Current strength in runs 1, 3b, and 3c suggests that this approximately represents the limit of strengthening that can be achieved by introduction of upper west Pacific warm water. However, the flows and surface heat loss in the Agulhas Current/outflow region are greatly increased in run 3c over run 3b, and now approach the run 1 values. Globally, the run 3c minus run 2 differences in the surface and midlevel fields are mostly quantitatively similar to run 1 minus run 2 differences (Figs. 1b, 13–15) and thus, are not shown. (Exceptions are the responses in the southwest Tasman Sea and Agulhas retroflexion south of Africa, which are weaker in the case of run 3c. Run 1 minus run 3c heat flux differences exceed $40 W m^{-2}$ in both regions.) However, run 3c minus run 2 streamfunction differences are mostly small, and so the perturbation surface flows of run 3b (similar to Fig. 14a) are largely offset by strong deep flows in the opposite direction. For example, Fig. 18 shows run 3c minus run 2 velocity differences at 2350 m (level 10). The clockwise deep flow offsets the basically counterclockwise mid- to upper-level flow perturbations. In contrast, the full throughflow case features small, deep velocities.

A pure baroclinic throughflow can fairly closely mimic the surface effects of the full throughflow but only if the sill depth over which the baroclinic throughflow occurs is very deep. However, pure baroclinic throughflow over even a shallow sill (run 3) is capable of major enhancement of the Leeuwin Current system.

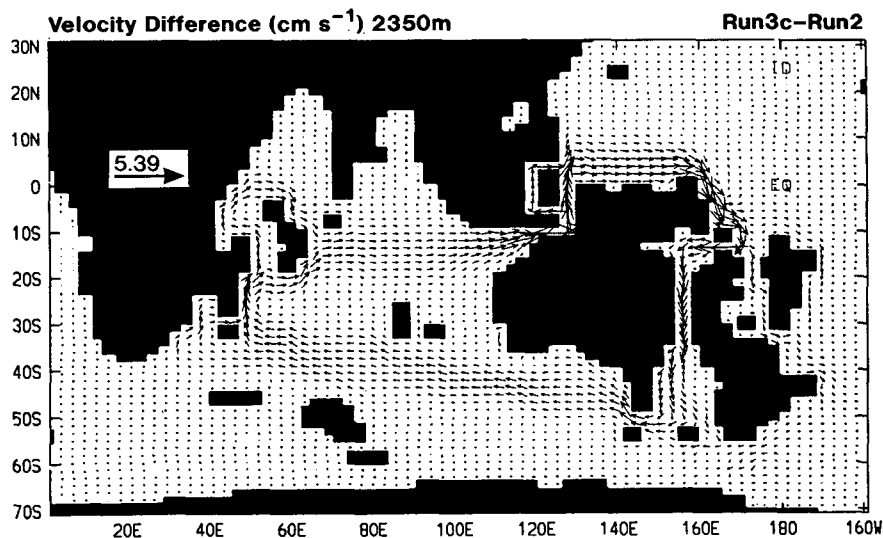


FIG. 18. Velocity differences for run 3c minus run 2 in the Indian/southwest Pacific region, at 2350 m (units: $cm s^{-1}$).

d. Cooled throughflow case

We complete our dissection of the throughflow by conducting a run (run 4) designed to minimize the effect of different Indian and Pacific density profiles on the Indian Ocean circulation, while retaining a wind-forced net throughflow. This run is identical to run 1, except that the temperature and salinity over area *A* (Fig. 19c) to 1250-m depth are relaxed towards profiles obtained from spatial averaging over area *B* (Fig. 6b) in the *no throughflow* case (run 2). The relaxation time is 20 days, compared to an estimated minimum time of 50 days for water to pass through area *A*. Thus, water entering the Indian Ocean has temperature and salinity profiles close to that achieved by the eastern Indian Ocean in isolation from the Pacific. Thereby, we effectively mitigate the pure baroclinic component of the throughflow.

Figure 19 shows the run 4 minus run 2 differences of (a) surface current, (b) current at 635 m, and (c) surface heat flux. The Indian Ocean response to the cool throughflow is the converse of that to the baroclinic throughflow (run 3). The Leeuwin Current system and associated surface heat loss are only slightly enhanced over that in run 2, while heat loss from the Agulhas Current/outflow is strongly enhanced and approaches run-1 values. The Agulhas Current and outflow strengthen at all levels above 1250 m (e.g., Fig. 19b), as for run 1. However, the additional flow for the deep portion of the Agulhas Current originates from downwelling in the Indonesian passages induced by the in situ cooling (Fig. 19b), unlike for run 1.

5. Discussion

a. Large-scale heat transports

This section discusses the effect of Indonesian throughflow on the large-scale oceanic transport of heat. When full throughflow is permitted, the southward heat transport is increased in the Indian Ocean and decreased in the South Pacific. However, total transports for the World Ocean plotted in Fig. 20 show that the two changes in heat transport do not balance. The Indian Ocean increase exceeds the South Pacific decrease by up to 0.3 petawatts (PW), or about 12% of the total oceanic heat transport. The difference in southward heat transport is largest between 10° and 25°S. The additional equatorial heating implied by Fig. 20 is provided by the extensive band of gain along the equatorial Pacific (Fig. 1b). South of 25°S, the heat losses in the Indian Ocean exceed the gains in the Pacific.

Interbasin changes in heat transport are much larger than the zonal average changes. Table 4 lists surface heat flux differences integrated over each of the three ocean regions shown on Fig. 1b. There is a net transfer of 0.62 PW out of the Pacific sector as a result of the full throughflow (this being approximately one third

of the total heat input into the model Pacific between 10°N and 10°S). Of this, 0.57 PW is lost to the atmosphere in the Indian Ocean sector. Much of the loss occurs in the Agulhas outflow: a net 0.36 PW is lost in the Indian Ocean sector between 35° and 50°S (i.e., 63% of total). The perturbation heat gain in the Pacific is more evenly distributed among several locations: the equatorial Pacific (10°N–10°S) gains 0.21 PW, the Tasman Sea (32°–50°S, 148°–165°E) gains 0.16 PW, and the South Pacific (35°–50°S, 170°E–70°W) gains 0.09 PW.

The total southward heat transport is also enhanced by the baroclinic throughflow of run 3 (Fig. 20), but only by a small margin (about 0.1 PW). Net interbasin exchanges are also smaller (Table 4). In this case, the zero mass transport allows direct calculation of net heat transport through the Indonesian passage. The southward heat transport across a line between the Java Peninsula and New Guinea is 0.31 PW. Thus, in this case, 75% of all heat transferred via the Indonesian passage is released to the atmosphere within the Indian Ocean sector; the remainder is recirculated back into the Pacific to the south of Tasmania.

Perturbation heat loss in the Atlantic sector is negligible for run 3. We note that Agulhas leakage in each of runs 2, 3, 3b, and 3c remains at 1 Sv. Thus, it is the barotropic component of the throughflow that leads to increased leakage and the small Atlantic perturbation heat loss in run 1 (Table 4).

b. Impact of real-world Indonesian throughflow

We now consider some possible impacts of the real world Indonesian throughflow on ocean circulation and climate, as suggested by the present model results. This requires some discussion of the likely realism of the model results. Recent observations (Godfrey 1989; Fieux et al. 1992) suggest that the annual-mean net transport of the actual throughflow is somewhat less than that in the present run 1 (perhaps 12 Sv versus 17 Sv). However, Fieux et al. (1992) also find evidence of return Indian to Pacific flow at depth, of strength a few Sv. Thus, the real throughflow may feature a weaker barotropic component but a significant baroclinic component. Consequently, the actual throughflow may have an effect intermediate between that in runs 1 and 3; namely a strong Leeuwin Current response but an Agulhas outflow and Tasman Sea response moderately weaker than that suggested by run 1. Further, the size (but not the sign) of the Tasman Sea response should be viewed with caution, because eddy dynamics are known to be very important in this region. Our model cannot reproduce these effects.

Seasonal variation in the upper boundary conditions, neglected in the present experiments, is likely to have at least two effects on the surface response. First, the surface response in the Southern Hemisphere midlatitudes is likely to be greatest in winter, when convective

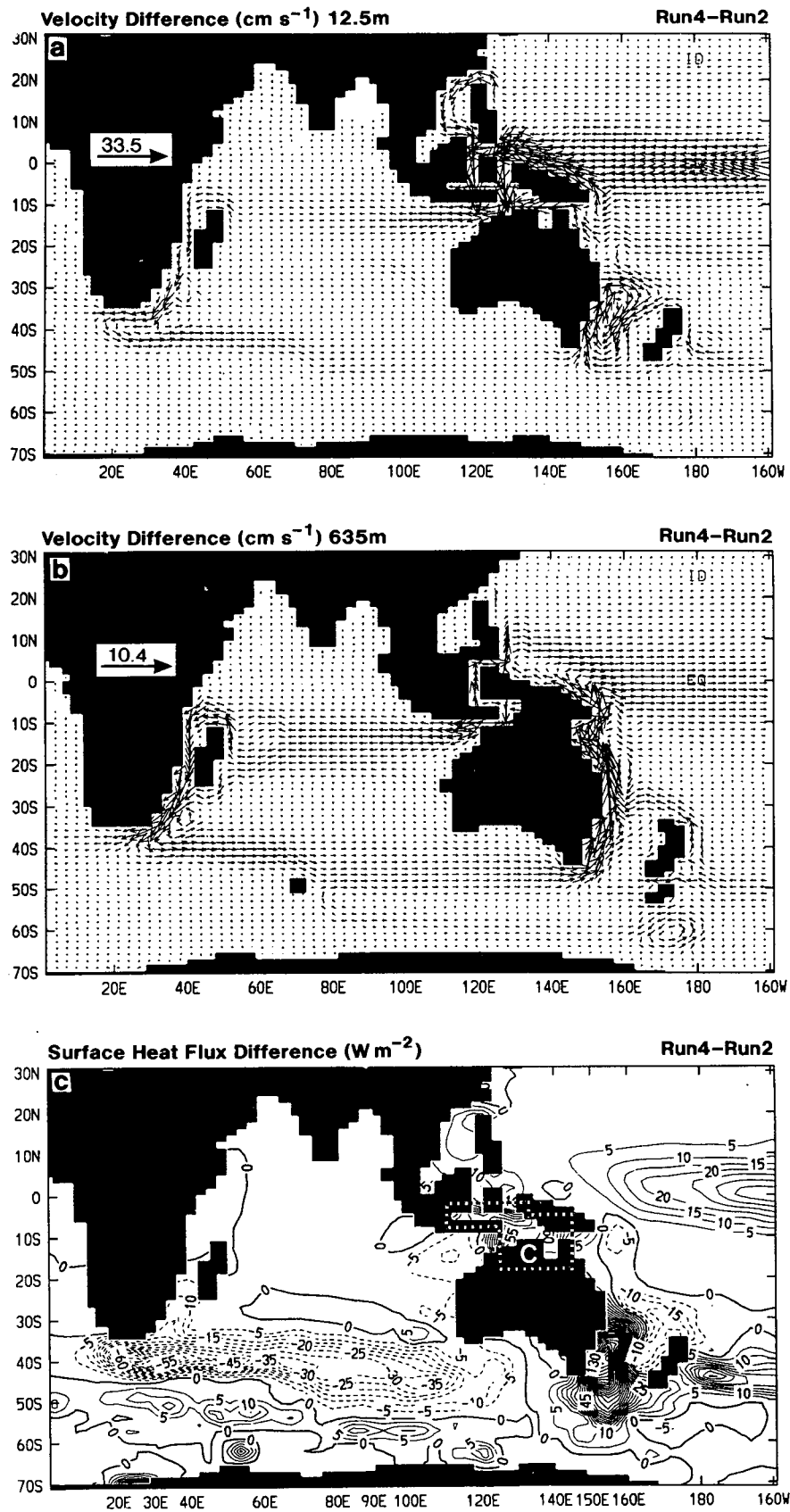


FIG. 19. Difference fields for run 4 minus run 2, in the Indian/southwest Pacific region: (a) velocity at 12.5 m (cm s^{-1}), (b) velocity at 635 m (cm s^{-1}), and (c) surface heat flux (W m^{-2}). Note different velocity scales on (a) and (b). Area C (referred to in text) is also shown in (c).

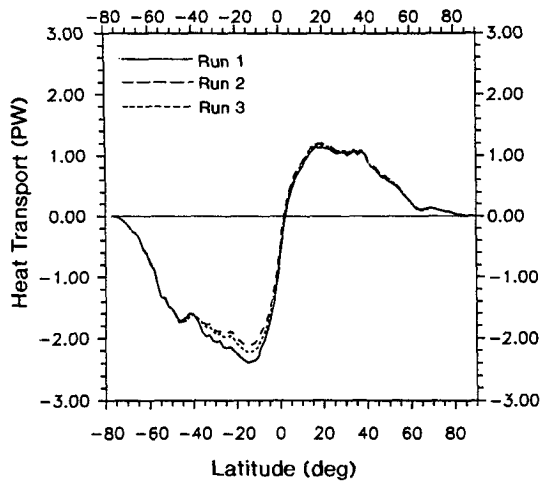


FIG. 20. Meridional heat transport zonally integrated about the globe for run 1 (solid), run 2 (long dash), and run 3 (short dash). Units are petawatts.

overturn is at its most active. Second, regions that experience strong seasonal upwelling/downwelling as a result of seasonally reversing winds may experience a strong surface response during the upwelling season, as subsurface perturbations are advected upward. An example may be the strong upwelling along the Somali and Arabian coasts during the summer monsoon, which contributes to the cooling of the northwest Indian Ocean at that time. This upwelling is only weakly represented in the present (annual-mean) experiments. The seasonal cooling would be probably stronger in the absence of throughflow, with possible consequences for the behavior of the Indian summer monsoon.

Possible climatic effects resulting from the warming of the Indian Ocean by the throughflow have been discussed in Godfrey (1989) and HWG. Here we note that the SST and surface heat flux perturbations over the central and northern Indian Ocean are very small in the present experiments and probably would be insufficient to cause significant climatic perturbation (however, note neglect of seasonal upwelling). The larger perturbations in the eastern Indian Ocean, the Agulhas outflow region, and the Tasman Sea are more likely to be climatically significant. Warming would occur in the African/Indian Ocean/Australian sector between about 30° and 50°S. In particular, southern Australia would be frequently downwind from the extensive fetch of the strengthened Agulhas outflow and also from the strengthened Leeuwin Current system during winter. The effect of the Agulhas outflow perturbation on rainfall patterns is less clear. However, the warmer water off northwest Australia may enhance precipitation over a large portion of Australia (e.g., Nicholls 1989). The southeast coast of Australia receives most of its year-round precipitation in association with moist easterly winds; the throughflow, via its cooling of the Tasman Sea, would be expected to result

in a cooler, more stable, onshore flow and thus, coastal precipitation less intense than otherwise.

The throughflow cools the central and eastern equatorial Pacific. The effect of such a lower climatological SST on ENSO is not clear; however, the strength, frequency, and even the mechanism of oscillation in coupled models is found to be very dependent on the background state (e.g., Hirst 1990). It remains to be seen whether ENSO is more or less vigorous under conditions of a generally cooler central and east Pacific (which may reduce the atmospheric response to given SST anomaly) but with enhanced horizontal and vertical temperature gradients (which increase the SST response to given wind anomaly).

Our use of relaxation-type upper boundary conditions with short decay times for temperature and salinity tends to localize those aspects of the response that exhibit a large surface expression. Thus, baroclinic wave and other deep advective responses are probably fairly insensitive to the form or decay time of the upper boundary conditions (provided stratification is stable), whereas responses linked to the surface by proximity or convective overturn may be more affected. Use of a longer decay time for surface temperature may tend to reduce the local intensity of the heat flux response but allow a larger surface area to be affected. Use of a constant flux condition for salinity should allow widespread advection of salinity perturbations, possibly as far as deep-water formation regions, and so affect deep-water formation rates. In particular, the small effect of the throughflow (in our model) on North Atlantic Deep Water formation rates may result from our restoration of North Atlantic surface salinities towards climatology. Thus, the present experiments are not suitable for testing the hypothesis of Gordon (1986) that heat and salt transports linked to the Indonesian throughflow play a major role in controlling NADW formation.

A comparison of the present results with those from the same model forced by a fixed salinity flux would be very instructive. However, results regarding NADW formation rates would still have to be viewed with caution, for two reasons. First, the dynamical control of Agulhas retroreflection and leakage in our model is primarily by viscous, and not inertial, effects (cf. De Ruijter 1982; Ou and De Ruijter 1986). Given that the dynamics of the model retroreflection is probably wrong, any results relating to changes in the volume of Agulhas leakage must be viewed with caution. Second, all the

TABLE 4. Change in downward surface heat flux integrated over each of the three ocean regions delineated in Fig. 1b. Units are in petawatts.

Region	Run 1-Run 2	Run 3-Run 2
(A) Pacific	+0.62	+0.23
(B) Indian	-0.57	-0.23
(C) Atlantic	-0.05	+0.01

present experiments feature a leakage that is too weak, presumably because of excessive viscosity and lack of eddies. Thus, most of the water for NADW formation in this model must originate from the fresh, cold water of Drake Passage. The small leakage may deemphasize Indonesian throughflow effects via the warm-water route. More generally, coarse-resolution GCMs that display such a weak leakage may have problems with the Atlantic circulation when coupled to an atmospheric GCM, unless a salt-flux correction is used.

6. Summary and concluding remarks

A series of model runs has been conducted to examine the effect of Indonesian throughflow on the ocean circulation and surface heat flux field in a general circulation model of the World Ocean. The principal runs are (i) Indonesian passage open and nonzero net throughflow permitted, (ii) Indonesian passage completely closed, (iii) Indonesian passage open but only pure baroclinic throughflow permitted (i.e., net throughflow is restrained to be identically zero), and (iv) Indonesian passage open but throughflow cooled and salted to profiles typical of the east Indian Ocean in isolation from the Pacific.

The effect of the full (17 Sv) throughflow on the Indian and Pacific oceans is summarized schematically in Fig. 21. The pathway of perturbation mass transport is depicted therein by arrows. The perturbation flow first proceeds westward across the Indian Ocean (as an enhancement of the South Equatorial Current) and is largely confined to the top 500 m. During its passage, this flow loses nearly half its mass (about 8 Sv) to southward outflow. This outflow enters a reverse flow directed back towards the east/southeast. The reverse flow descends via enhanced downwelling, mainly at the west Australian coast, in turn feeding an undercurrent that returns back towards Madagascar. The

Agulhas Current is strengthened, both above 500-m depth by the remaining direct flow (~ 9 Sv) from the Indonesian passage and below 500-m depth by the return flow (~ 8 Sv) from the downwelling off western Australia. Substantial perturbation transport then occurs both above and below 500 m along the course of the Agulhas Current/outflow, to the south of Australia, and finally up the Australian east coast, in a counter-clockwise pattern consistent with Munk (1950) dynamics. In the tropical Pacific, the deep portion of this flow separates from the coast and forms a broad eastward flow, which eventually fans out into the extratropics in the eastern basin. Weak perturbation upwelling is widespread in the tropical and eastern Pacific, but is strongest along parts of the American west coast. The upwelling feeds a return upper flow, which finally joins the upper perturbation flow proceeding directly towards the Indonesian passage along the Australia/New Guinea east coast. A total of about 10 Sv participates in the basinwide Pacific upwelling.

Thus, the actual mass transport path is rather more complicated than that indicated by the depth-integrated transport alone (Fig. 11a). Pure baroclinic flows are associated with downwelling off western Australia and upwelling in the Pacific, thereby facilitating extension of the initially shallow mass transport to much greater depth. The baroclinic flows are also essential to the involvement of the Pacific basin at large.

The main thermal response features a general warming of the upper Indian Ocean and cooling of the upper Pacific Ocean. The largest temperature perturbations are usually found in the main thermocline. In contrast, changes in surface temperature and heat flux are very small over most of both oceans. Only in regions affected by strong upwelling or convective mixing are the subsurface temperature perturbations brought upward and the surface heat flux strongly affected. In the Indian Ocean, perturbation heat loss occurs primarily

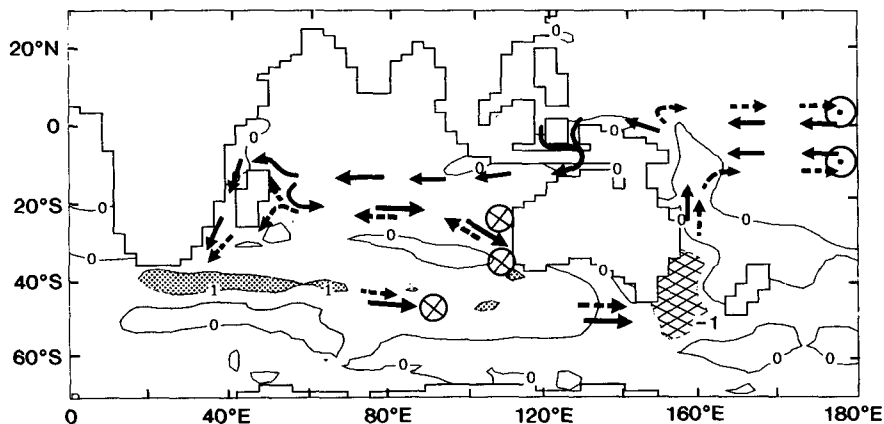


FIG. 21. Schematic of general ocean response to the throughflow. Solid and dashed arrows indicate perturbation currents near the surface (0–500-m depth) and at depth (500–1800 m), respectively. Shading and hatching indicate SST perturbation in excess of $+1^\circ$ and -1°C , respectively; the zero contour is also shown. Circle with interior cross indicates downwelling, with interior dot indicates upwelling.

in the Agulhas Current and outflow and secondarily near western Australia in the vicinity of the Leeuwin Current. In the Pacific Ocean, most of the perturbation heat gain occurs in (i) the Tasman Sea, (ii) the upwelling zones along the equator and the American coast, and (iii) two regions of convective mixing in the far South Pacific. In net, 0.62 PW of heat is transferred from the Pacific, of which 0.57 PW is released to the atmosphere in the Indian Ocean.

The third and fourth runs were conducted to study the effects of the buoyancy-driven and barotropic components of the throughflow in isolation. The third run features a Pacific to Indian flow of upper-level water (0–300-m depth) and an equal return flow below, transferring a relatively small net 0.23 PW of heat to the Indian Ocean. Nevertheless, changes of heat flux in the Leeuwin Current region are almost as strong as for the full throughflow. Otherwise, the oceanic response is much weaker than in the full throughflow case, though the patterns of surface temperature and upper-current change are qualitatively similar to that in Fig. 21. The fourth run, featuring the cooled throughflow, exhibits a response that is the converse of that for the third run; namely, the Agulhas response is nearly as strong as the full throughflow, but the Leeuwin Current response is very weak.

The results for all the runs are broadly consistent with those of McCreary and Kundu (1984), who found that Leeuwin Current-like features in their idealized model were strengthened as the throughflow was made shallower. They explained this result in terms of the projection of the throughflow onto damped baroclinic internal modes. The pattern of the present response suggests that baroclinic mode dynamics are also very important here. However, further discussion of the dynamics behind the subsurface temperature response is postponed until after study of the transient response to a change in Indonesian throughflow, in Hirst and Godfrey (1993).

Acknowledgments. The authors would like to thank Drs. R. L. Hughes and A. M. Moore for constructive review of a preliminary draft. Helpful discussions with the above and also Drs. N. R. Smith and A. J. Weaver are acknowledged. Thanks also to W. J. Cai and J. V. Mansbridge for assistance with programming and graphics. We are indebted to the late Michael Cox, who generously provided us with the basic code for the model. The computations were carried out on the CRAY-YMP-2 at the Joint Supercomputer Facility, Port Melbourne, Victoria. This research was partly funded by the Wool Research and Development Corporation of Australia.

APPENDIX

Effect of Acceleration Techniques

One potential problem with the acceleration techniques of Bryan (1984) is that they are strictly appli-

cable only for finding *temporally constant* solutions, yet we have noted (section 3) the persistence of weak transients in our solutions. Another potential problem is that the conservation rule for the volume integral of tracer Q ($I = \sum Q_{ijk} V_{ijk}$) under advection and internal diffusion is broken when the tracer time step has depth dependence. Instead, the nonphysical quantity $I_1 = \sum \gamma_k Q_{ijk} V_{ijk}$ is conserved, where V_{ijk} is the volume of the ijk th cell and γ_k is the ratio of the time step at level k to the time step at level 1. This explains the nonconservation of tracers in some models forced with flux upper boundary conditions, even though the surface integral of the flux is zero (e.g., Weaver and Sarachik 1991). This nonconservation should not be a major problem for models subject to restoring upper boundary conditions. Nevertheless, we tested the sensitivity of the solution to depth-dependent time stepping by restarting the model from the final solutions of both runs 1 and 2 and then running the model in both cases for an additional 24 000 steps (100 years) with the tracer time step set to 1.5 days at all levels. Changes in the solution were negligible, and overall rates of change remained well within the convergence criteria of section 3.

REFERENCES

- Bryan, F., 1987: Parameter sensitivity of primitive equation ocean general circulation models. *J. Phys. Oceanogr.*, **17**, 970–985.
- Bryan, K., 1969: A numerical method for the study of the circulation of the World Ocean. *J. Comput. Phys.*, **4**, 347–376.
- , 1984: Accelerating the convergence to equilibrium of ocean-climate models. *J. Phys. Oceanogr.*, **14**, 666–673.
- , and M. D. Cox, 1972: An approximate equation of state for numerical models of ocean circulation. *J. Phys. Oceanogr.*, **2**, 510–514.
- , and L. J. Lewis, 1979: A water-mass model of the World Ocean. *J. Geophys. Res.*, **84**, 347–376.
- Colborn, J. G., 1975: *The Thermal Structure of the Indian Ocean*. University of Hawaii Press, 173 pp.
- Cox, M. D., 1975: A baroclinic numerical model of the World Ocean: Preliminary results. *Numerical Models of Ocean Circulation*, Natl. Acad. Sci., 107–118.
- , 1984: A primitive equation, 3-dimensional model of the ocean. GFDL Ocean Group Tech. Rep. No. 1, GFDL/Princeton University, 141 pp.
- , 1987: GFDL Ocean Model Circular No. 8. GFDL/Princeton University, 2 pp.
- Cresswell, G. R., and T. J. Golding, 1980: Observations of a south-flowing current in the southeastern Indian Ocean. *Deep-Sea Res.*, **27**, 449–466.
- De Ruijter, W. P. M., 1982: Asymptotic analysis of the Agulhas and Brazil Current System. *J. Phys. Oceanogr.*, **12**, 361–373.
- Esbensen, S. K., and V. Kushnir, 1981: The heat budget of the global ocean: An atlas based on estimates from surface marine observations. Rep. 29, Climatic Research Institute, Oregon State University, 27 pp.
- England, M. H., 1992: On the formation of Antarctic Intermediate and Bottom Water in ocean general circulation models. *J. Phys. Oceanogr.*, **22**, 918–926.
- Fioux, M., C. Andrié, P. Delecluse, A. G. Ilahude, A. Kartavtseff, F. Mantisi, R. Molcard, and J. C. Swallow, 1992: Measurements within the Pacific–Indian oceans throughflow region; preliminary results of the JADE cruise. *Deep-Sea Res.*, in press.
- Gates, W. L., and A. B. Nelson, 1975: A new (revised) tabulation of the Scripps topography on a 1° global grid. Part I: Terrain

- Heights. Tech. Rep. R-1276-1-ARPA, The Rand Corporation, 132 pp.
- Godfrey, J. S., 1989: A Sverdrup model of the depth-integrated flow for the World Ocean allowing for Island Circulations. *Geophys. Astrophys. Fluid Dyn.*, **45**, 89–112.
- , and T. J. Golding, 1981: The Sverdrup relation in the Indian Ocean and the effect of the Pacific–Indian oceans throughflow on Indian Ocean circulation and on the east Australian Current. *J. Phys. Oceanogr.*, **11**, 771–779.
- , and K. R. Ridgeway, 1985: The large-scale environment of the poleward-flowing Leeuwin Current, western Australia: Long-shore steric-height gradients, wind stresses and geostrophic flow. *J. Phys. Oceanogr.*, **15**, 481–494.
- , and A. J. Weaver, 1991: Is the Leeuwin Current driven by Pacific heating and winds? *Progress in Oceanography*, Vol. 27, Pergamon, 225–272.
- Gordon, A. L., 1986: Inter-ocean exchange of thermocline water. *J. Geophys. Res.*, **91**, 5037–5046.
- Hamon, B. V., 1965: Geostrophic currents in the southeastern Indian Ocean. *Aust. J. Mar. Freshwater Res.*, **16**, 255–271.
- Han, Y.-J., 1984: A numerical World Ocean general circulation model. Part II. A baroclinic experiment. *Dyn. Atmos. Oceans*, **8**, 141–172.
- Hellerman, S., and M. Rosenstein, 1983: Normal monthly wind stress over the World Ocean with error estimates. *J. Phys. Oceanogr.*, **13**, 1093–1104.
- Hirst, A. C., 1990: On simple coupled ocean–atmosphere models, equatorial instabilities, and ENSO. *Int. TOGA Scientific Conf. Proc. (Invited Papers)*. Honolulu, 103–110.
- , and J. S. Godfrey, 1993: The response to a sudden change in Indonesian Throughflow in a global ocean GCM. *J. Phys. Oceanogr.*, **23**, 300–328.
- Hsuing, J., 1985: Estimates of global oceanic meridional heat transport. *J. Phys. Oceanogr.*, **15**, 1405–1413.
- Hughes, T., A. J. Weaver, and J. S. Godfrey, 1992: Thermohaline forcing of the Indian Ocean by the Pacific Ocean. *Deep-Sea Res.*, **39**, 965–996.
- Hunter, J. R., and C. J. Hearn, 1988: On the convolution method of describing bottom friction in depth-averaged models. *J. Phys. Oceanogr.*, **18**, 1752–1754.
- Kindle, J. C., H. E. Hurlburt, and E. J. Metzger, 1989: On the seasonal and interannual variability of the Pacific to Indian Ocean throughflow. *Western Pacific Int. Meeting and Workshop on TOGA COARE*. Noumea, New Caladonia, 833 pp.
- Levitus, S., 1982: *Climatological atlas of the World Ocean*. NOAA Prof. Paper 13, U.S. Govt. Printing Office, Washington, D.C., 173 pp.
- Luyten, J., and H. Stommel, 1986: Gyres driven by combined wind and buoyancy flux. *J. Phys. Oceanogr.*, **16**, 1551–1560.
- Maier-Reimer, E., U. Mikolajewicz, and T. Crowley, 1990: Ocean general circulation model experiment with an open Central American isthmus. *Paleoceanogr.*, **5**, 349–366.
- Manabe, S., and R. J. Stouffer, 1988: Two stable equilibria of a coupled ocean–atmosphere model. *J. Climate*, **1**, 841–866.
- Marotzke, J., 1991: Influence of convective adjustment on the stability of the thermohaline circulation. *J. Phys. Oceanogr.*, **21**, 903–907.
- McCreary, J. P., and P. K. Kundu, 1986: On the dynamics of the throughflow from the Pacific to the Indian Ocean. *J. Phys. Oceanogr.*, **16**, 2191–2198.
- Munk, W. H., 1950: On the wind-driven ocean circulation. *J. Meteor.*, **7**, 79–93.
- Nicholls, N., 1989: Sea surface temperature and Australian winter rainfall. *J. Climate*, **2**, 965–973.
- Ou, H. W., and W. P. M. De Ruijter, 1986: Separation of an inertial boundary current from a curved coastline. *J. Phys. Oceanogr.*, **16**, 280–289.
- Reynolds, R. W., and L. Roberts, 1987: A global sea surface temperature climatology from in situ, satellite and ice data. *Trop. Ocean–Atmos. Newslett.*, **37**, 15–17.
- Seager, R., S. E. Zebiak, and M. A. Cane, 1988: A model of the tropical Pacific sea surface temperature climatology. *J. Geophys. Res.*, **93**, 1265–1280.
- Semtner, A. J., and R. M. Chervin, 1988: A simulation of the global ocean circulation with resolved eddies. *J. Geophys. Res.*, **93**, 15 502–15 522.
- Talley, L. D., 1984: Meridional heat transport in the Pacific Ocean. *J. Phys. Oceanogr.*, **14**, 231–241.
- Thompson, R. O. R. Y., 1984: Observations of the Leeuwin Current off Western Australia. *J. Phys. Oceanogr.*, **14**, 623–628.
- Toggweiler, J. R., K. Dixon, and K. Bryan, 1989: Simulations of radiocarbon in a coarse-resolution World Ocean model. 1: Steady state prebomb distributions. *J. Geophys. Res.*, **94**, 8217–8242.
- Weaver, A. J., and J. F. Middleton, 1989: On the dynamics of the Leeuwin Current. *J. Phys. Oceanogr.*, **19**, 626–648.
- , and E. S. Sarachik, 1991: The role of mixed boundary conditions in numerical models of the ocean's climate. *J. Phys. Oceanogr.*, **21**, 1470–1493.
- Welander, P., 1986: Thermohaline effects in the ocean circulation and related simple models. *Large-scale Transport Processes in Oceans and Atmosphere*, D. L. T. Anderson and J. Willebrand, Eds., NATO ASI series, Reidel, 163–200.
- Wyrtki, K., 1962: Geopotential topographies and associated circulation in the south-eastern Indian Ocean. *Aust. J. Mar. Freshwater Res.*, **13**, 1–17.